ARTICLES
https://doi.org/10.1038/s41567-021-01360-7
nature physics

Check for updates

Fluctuating hydrodynamics of chiral active fluids

Ming Han[1,2], Michel Fruchart[1,3], Colin Scheibner[1,3], Suriyanarayanan Vaikuntanathan[1,4], Juan J. de Pablo[2,5] and Vincenzo Vitelli[1,3,6] ✉

Active materials are characterized by continuous injection of energy at the microscopic level and typically cannot be adequately described by equilibrium thermodynamics. Here we study a class of active fluids in which equilibrium-like properties emerge when fluctuating and activated degrees of freedom are statistically decoupled, such that their mutual information is negligible. We analyse three paradigmatic systems: chiral active fluids composed of spinning frictional particles that are free to translate, oscillating granular gases and active Brownian rollers. In all of these systems, a single effective temperature generated by activity parameterizes both the equation of state and the emergent Boltzmann statistics. The same effective temperature, renormalized by velocity correlations, relates viscosities to steady-state stress fluctuations via a Green–Kubo relation. To rationalize these observations, we develop a theory for the fluctuating hydrodynamics of these non-equilibrium fluids and validate it through large-scale molecular dynamics simulations. Our work sheds light on the microscopic origin of odd viscosities and stress fluctuations characteristic of parity-violating fluids, in which mirror symmetry and detailed balance are broken.

Granular media have long been a playground for children and statistical physicists alike[1–3]. Here, we consider a class of non-equilibrium fluids exemplified by frictional grains constantly spinning in a plane. Typically, two grains of sand would only lose energy by friction when they collide. By contrast, spinning particles can also gain energy after a collision, if their rotation speed is rapidly reset to a constant value by microscopic torques or external fields. A collection of many such particles, all spinning in the same direction (clockwise or anticlockwise), is often referred to as a chiral active fluid[4–13]. Experimental realizations include colloidal particles[4,11,14], robots[10] and even living systems[15,16]. In this article, we use non-equilibrium statistical mechanics to develop a fluctuating hydrodynamic theory for chiral active fluids: a continuum theory that describes both the macroscopic behaviour of the fluid and its fluctuations in one go. This allows us to describe phenomena ranging from steady-state velocity fluctuations to non-linear shock propagation.

Despite being driven and dissipative, chiral active fluids share several aspects with equilibrium fluids when their spinning speed is nearly constant and uniform. They display a Maxwell–Boltzmann probability distribution and an equation of state, and their viscous response satisfies a fluctuation–response relation. The same viscous response bears signatures of their non-equilibrium character through the existence of so-called odd viscosities that can only occur when detailed balance is broken. These equilibrium-like behaviours occur when the activated and fluctuating degrees of freedoms are statistically decoupled, a feature that we shall see extends beyond chiral active fluids to other systems such as oscillating granular gases[17–19] and active Brownian rollers[20,21].

Microscopic model of a chiral active fluid

We start by considering a simplified microscopic model of a two-dimensional chiral active fluid (Fig. 1a and Supplementary Videos S1–S3) composed of athermal frictional particles all spinning in the same direction[4–8,10–12]. In order to impart a fixed chirality to the system, we incorporate active torques into a standard model of granular disks (see Methods and ref. [22]). The positions $\mathbf{x}_i$ of the particles and their angular velocities $\mathbf{\Omega}_i$ then follow the equations of motion

$$m\ddot{\mathbf{x}}_i = \sum_{j\in N(i)} \mathbf{f}_{ij} \tag{1}$$

$$I\dot{\mathbf{\Omega}}_i = \boldsymbol{\tau}_i + \sum_{j\in N(i)} \mathbf{r}_{ij}\times\mathbf{f}_{ij} \tag{2}$$

in which m is the mass of the particles and I their moment of inertia. Each particle i interacts with its neighbours $j\in N(i)$ closer than its diameter d through a force

$$\mathbf{f}_{ij} = \underbrace{-k(d-r_{ij})\hat{\mathbf{r}}_{ij}}_{\mathbf{f}_{ij}^{\mathrm{c}}} + \underbrace{\gamma(-\mathbf{v}_{ij}+\mathbf{\Omega}_{ij}\times\mathbf{r}_{ij})}_{\mathbf{f}_{ij}^{\mathrm{nc}}} \tag{3}$$

in which the central force $\mathbf{f}_{ij}^{\mathrm{c}}$ models a soft repulsion between the disks while the non-central force $\mathbf{f}_{ij}^{\mathrm{nc}}$ models interparticle friction (Fig. 1a). Particles i and j are separated by a vector $\mathbf{r}_{ij}=\mathbf{x}_i-\mathbf{x}_j=r_{ij}\hat{\mathbf{r}}_{ij}$, the difference between their velocities $\mathbf{v}_k=\dot{\mathbf{x}}_k$ is $\mathbf{v}_{ij}=\mathbf{v}_i-\mathbf{v}_j$, and the average rotation speed of a pair of particles is $\mathbf{\Omega}_{ij}=\hat{\mathbf{z}}\,(\Omega_i+\Omega_j)/2$. In addition, each particle experiences an active torque $\boldsymbol{\tau}_i=\gamma_{\mathrm{rot}}(\Omega-\Omega_i)\hat{\mathbf{z}}$ that tends to maintain a constant angular velocity $\Omega_i\approx\Omega$. When γ_{rot} is large, Ω_i relaxes to Ω faster than other time scales in the system, allowing the rotational degrees of freedom (that we call 'activated') to act as an effective bath for the translational ones (that we call 'fluctuating'). Hence, one can replace $\mathbf{\Omega}_{ij}\to\Omega\,\hat{\mathbf{z}}$ in equation (1) while eliminating equation (2). Crucially, the non-central force $\mathbf{f}_{ij}^{\mathrm{nc}}$ violates parity: equation (1) is not invariant under the mirror reflection $x,y\to-x,y$ when $\Omega\neq0$ (the system is chiral).

Effective temperature

We conduct molecular dynamics simulations of the chiral active fluid described by equation (1) in this limit. Despite being athermal and driven, the active fluid exhibits a single effective temperature

[1]James Franck Institute, University of Chicago, Chicago, IL, USA. [2]Pritzker School of Molecular Engineering, University of Chicago, Chicago, IL, USA. [3]Department of Physics, University of Chicago, Chicago, IL, USA. [4]Department of Chemistry, University of Chicago, Chicago, IL, USA. [5]Center for Molecular Engineering, Argonne National Laboratory, Lemont, IL, USA. [6]Kadanoff Center for Theoretical Physics, University of Chicago, Chicago, IL, USA. ✉e-mail: vitelli@uchicago.edu

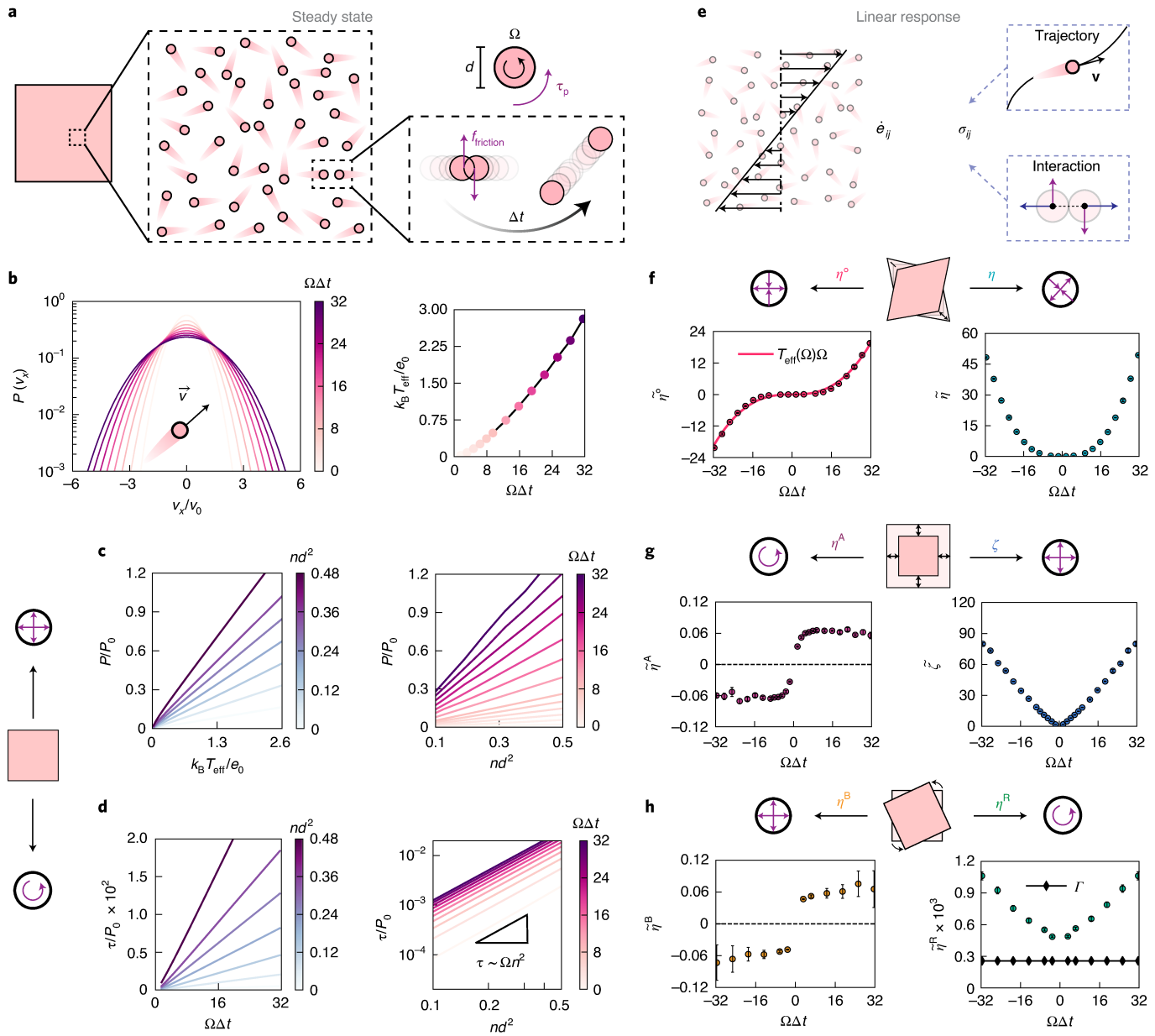

Fig. 1 | Steady-state and linear response of a chiral active fluid. a, Schematic of a granular gas. We simulate a 2D granular gas composed of frictional particles with diameter d, which are powered by an active torque τ_p to self-spin at a constant speed Ω. During collision, two self-spinning particles slide with respect to each other. The resultant interparticle friction causes transverse motion of the particles upon separation (Supplementary Video S1). $\Delta t = \sqrt{m/k}$ is a proxy for the average collision duration. **b**, Velocity distribution. The x-component of translational velocity follows a Gaussian distribution $P(v_x)$ at various spinning speeds Ω. An effective temperature T_{eff} is defined using the variance of v_x. The dependence of T_{eff} on Ω is shown on the right. **c**,**d**, Equations of state. At steady state, this system acquires an effective pressure P that satisfies the ideal gas law, $P = nk_BT_{\mathrm{eff}}$, where n is particle density. Unlike thermal systems, it also acquires a non-vanishing torque density τ that satisfies the relation $\tau \sim \Omega n^2$. **e**, Schematic of rheological measurements. We perturb the system with a velocity gradient $\dot{e}_{k\ell} = \partial_\ell u_k$ and measure the stress σ_{ij} to infer the viscosity tensor $\eta_{ijk\ell}$. The stress is calculated in the bulk from particle trajectory and interactions using the Irving–Kirkwood formula (7). This method can be applied to either simulation or experimental data. In the dilute limit, the kinetic part of the Irving–Kirkwood formula dominates, so the stress tensor can be determined purely from movies of particle motion, without knowledge of microscopic interactions. **f**, Odd and shear viscosities. A pure shear induces shear stress s_1 (⊕) via odd viscosity η° and shear stress s_2 (⊗) via shear viscosity η. **g**. Compression–rotation and bulk viscosities. A dilation/compression alters the torque density τ (↺) via a compression–rotation viscosity η^A and the pressure P (⊕) via the bulk viscosity ζ. **h**, Rotation–compression and rotation–rotation viscosities. A rotation changes the pressure P (⊕) via a rotation–compression viscosity η^B and the torque density τ (↺) via a rotation–rotation viscosity η^R. The coefficient $\Gamma = \tau/\Omega$ is plotted for comparison. The dependences of all the viscosities on spinning speed Ω are shown in **f**–**h**. The diagonal terms η, ζ and η^R in equation (6) are even in Ω, while η^A, η^B and η° are odd in Ω. Besides, $\eta^A(\Omega) = -\eta^B(-\Omega)$. All the viscosities $\tilde{\eta}_a = \eta_a/\eta_0$ are in units of $\eta_0 = m/d\Delta t$. We define $v_0 = d/\Delta t$, $e_0 = md^2/\Delta t^2$ and $P_0 = m/[d\Delta t^2]$. Unless otherwise specified, the number density is $nd^2 = 0.254$. Error bars denote standard errors.

T_{eff} that controls three properties typically associated with thermal equilibrium: (i) a Maxwell distribution of particle velocities (Fig. 1b), (ii) a nearly Boltzmann distribution of particle concentration in the presence of an external potential (Supplementary Figs. S1–S3) and (iii) an ideal gas equation of state (Fig. 1c). Similar properties emerge in oscillating granular gases (in which z translations are

activated while (x, y) translations are fluctuating; Methods, Extended Fig. E1 and Supplementary Videos S4 and S5) and fluids of active Brownian rollers (in which translations are activated and rotations are fluctuating; Extended Fig. E2 and Supplementary Videos S6 and S7). In both cases, an effective thermodynamic description emerges when the corresponding activated and fluctuating degrees of freedom are statistically decoupled.

The emergence of an effective temperature in the chiral active fluid can be captured by a mean-field approximation. As the interparticle vector $\hat{\mathbf{r}}_{ij}$ is random, the term $\boldsymbol{\Omega}_{ij} \times \hat{\mathbf{r}}_{ij}$ in equation (1) can be replaced by a white noise whose temperature is determined self-consistently (Supplementary Sect. II). As a result, the fluid follows a Langevin dynamics similar to a thermal fluid

$$m\ddot{\mathbf{x}}_i = \sum_{j\in N(i)} \mathbf{f}_{ij}^{\mathrm{c}} - \gamma_{\mathrm{eff}}\mathbf{v}_i + \tilde{\boldsymbol{\xi}}(t) \tag{4}$$

in which T_{eff} can be seen as the temperature of the effective bath. We show in Supplementary Sect. II that $\gamma_{\mathrm{eff}} = n\pi d^2\gamma$ and $\langle\tilde{\xi}_a(t)\tilde{\xi}_b(t')\rangle = 2\gamma_{\mathrm{eff}}k_{\mathrm{B}}T_{\mathrm{eff}}\delta_{ab}\delta(t-t')$ (see also Supplementary Fig. S4). In the chiral active fluid, the thermal exchange with a bath is replaced with an exchange of kinetic energy between rotational and translational degrees of freedom during collisions (Fig. 1a). Once a collision is over, the rotational speed Ω_i of each spinning particle is rapidly restored to Ω by the active torques $\boldsymbol{\tau}_i$. This process leads to a net gain or loss of energy until the translational degrees of freedom reach the effective temperature $T_{\mathrm{eff}}(\Omega)$ at which gain and loss are balanced on average. We show in Supplementary Sect. II that, in this case, $T_{\mathrm{eff}} \propto |\Omega|^{\alpha}$, where α is a non-universal exponent depending on $\mathbf{f}_{ij}^{\mathrm{c}}$ with $4/3 \leq \alpha \leq 2$. Consistent with this prediction, simulations with a contact potential reveal a power-law behaviour $T_{\mathrm{eff}} \propto |\Omega|^{1.54\pm0.02}$ over two decades. We emphasize that the mean-field approximation in equation (4) only captures single-particle properties controlled by T_{eff}, but not the breaking of detailed balance. Hence, equation (1) is still needed to fully account for the transport properties, such as viscosities, that are affected by the parity-violating nature of collisions illustrated in Fig. 2.

Chiral hydrodynamics

The evolution of the velocity field $\mathbf{u}$ of the chiral active fluid is described by the Navier–Stokes equation

$$\rho \mathrm{D}_t\mathbf{u} = \nabla\cdot\boldsymbol{\sigma} + \mathbf{f}_{\mathrm{vol}} \tag{5}$$

in which $\mathrm{D}_t = \partial_t + u_a\partial_a$ is the material derivative, $\boldsymbol{\sigma}$ is the stress tensor, $\mathbf{f}_{\mathrm{vol}}$ are external body forces and $\rho = nm$ is the mass density (n is the number density). The stress tensor $\boldsymbol{\sigma}$ in equation (5) is composed of a steady-state part $\boldsymbol{\sigma}^{\mathrm{ss}}$ present even in the absence of any velocity gradient, and a viscous part $\sigma_{ab}^{\mathrm{vis}} = \eta_{abcd}\,\partial_d u_c$, where η_{abcd} is the viscosity tensor of the fluid. The viscous stress $\sigma_{ab}^{\mathrm{vis}}$ describes surface forces between fluid layers that arise in response to velocity gradients. It is convenient to express the stress σ_{ab} and the unsymmetrized strain rate $\dot{e}_{cd} = \partial_d u_c$ as two vectors σ_α and $\dot{e}_\beta$, respectively, so that η_{abcd} can be represented as a matrix $\eta_{\alpha\beta}$ (see Methods and refs. [23,24]). For an isotropic two-dimensional fluid, the constitutive relation between stress and strain rate reads

$$\begin{pmatrix} \oplus \\ \circlearrowleft \\ \oplus \\ \otimes \end{pmatrix} = \begin{pmatrix} -P \\ -\tau \\ 0 \\ 0 \end{pmatrix} + \begin{pmatrix} \zeta & \eta^{\mathrm{B}} & 0 & 0 \\ \eta^{\mathrm{A}} & \eta^{\mathrm{R}} & 0 & 0 \\ 0 & 0 & \eta & \eta^{\mathrm{o}} \\ 0 & 0 & -\eta^{\mathrm{o}} & \eta \end{pmatrix} \begin{pmatrix} \dot{} \\ \dot{} \\ \dot{} \\ \dot{} \end{pmatrix} \tag{6}$$

$\sigma_\alpha \qquad \sigma_\alpha^{\mathrm{ss}} \qquad \eta_{\alpha\beta} \qquad \dot{e}_\beta$

The velocity gradients $\dot{e}_\beta$ are decomposed into dilation, rotation and two pure shears and at 45° of each other, while the stress σ_α is decomposed into pressure $\oplus$, torque $\circlearrowleft$ and two shear stresses $\oplus$ and $\otimes$ (see Methods for explicit expressions).

We performed large-scale molecular dynamics simulations to determine both the equations of state of the chiral active fluid in the steady state and its viscous response to velocity gradients (Fig. 1e). In the simulations, the stress tensor $\boldsymbol{\sigma}$ is determined using the Irving–Kirkwood formula[25]

$$\sigma_{ab} = -\frac{1}{A}\left[\sum_i m v_i^a v_i^b + \frac{1}{2}\sum_{i\neq j} f_{ij}^a r_{ij}^b\right] \tag{7}$$

that expresses the stress tensor $\boldsymbol{\sigma}$ in terms of the trajectories of the individual particles and their microscopic interactions. Here, A is the total area of the system, i, j label particles and a, b label spatial directions. The first term in equation (7) is called the kinetic part, while the second is called the virial part. We find that, in addition to a standard isotropic pressure P following the ideal gas law $P = nk_{\mathrm{B}}T_{\mathrm{eff}}$ (Fig. 1c), the steady-state stress tensor $\boldsymbol{\sigma}^{\mathrm{ss}}$ exhibits an anti-symmetric part (odd stress) corresponding to the net torque density $\tau = \Gamma(n)\,\boldsymbol{\Omega}$ with a density-dependent rotational friction coefficient $\Gamma(n) \sim n^2$ (Fig. 1d and Extended Fig. E3). This anti-symmetric stress would not arise from purely radial pairwise interactions between the particles, even if they were subject to microscopic torques[26]. Instead, it is a hydrodynamic manifestation of the transverse part of the force $\mathbf{f}_{ij}$ in equation (3). To see this, let us compute from equation (7) the anti-symmetric part of the Irving–Kirkwood stress (corresponding to the second line in equation (6))

$$\sigma_{ab} - \sigma_{ba} = \epsilon_{ab}\left[\frac{1}{2A}\sum_{i\neq j}\mathbf{r}_{ij}\times\mathbf{f}_{ij}\right] \tag{8}$$

in which only the virial part contributes as $v_i^a v_i^b = v_i^b v_i^a$. This shows that pairwise interactions can only contribute to the anti-symmetric part of the stress when they are not central (that is, when $\mathbf{r}_{ij}\times\mathbf{f}_{ij} \neq 0$). The force $\mathbf{f}_{ij}$ in equation (3) is short-ranged, so it affects the system only during collisions. Since the collision rate scales with the square of the density n, the cumulative effect of the gear-like frictional forces results in the observed $\Gamma(n) \sim n^2$.

Linear response with parity-violating viscosities

All the entries of the viscosity matrix were determined by deforming the simulation box at constant strain rate using the SLLOD algorithm[27]. The results (Fig. 1f–h and Supplementary Figs. S5–S7) are consistent with the general form in equation (6) imposed by isotropy. In addition to the standard shear and bulk viscosities η and ζ, we observe additional viscosity coefficients allowed by the broken time reversal and parity. First, a coefficient η^{o} known as odd (or Hall) viscosity[9,11,24,28–35] couples the two shear stresses. The ratio η^{o}/η, of order 1, is directly related to the angle $\overline{\alpha}$ defined in Fig. 2. This angle characterizes the average chirality of the collisions, which arises from the parity-violating interaction $\mathbf{f}_{ij}^{\mathrm{nc}}$ in equation (1). In addition, we find other parity-violating viscosities η^{A} and η^{B} that couple compression and rotation, and have smaller but non-zero magnitudes. Besides, there is a viscous contribution $\eta^{\mathrm{R}}\omega$ to the anti-symmetric stress, where $\omega = \dot{\circlearrowleft}$ is the vorticity. In an equilibrium fluid, we would have $\eta^{\mathrm{R}} = -\Gamma$ (refs. [26,36]), but this is not the case here (Fig. 1h). As they lead to an anti-symmetric stress, the coefficients η^{A}, η^{R} and Γ can only come from the virial contribution to the Irving–Kirkwood stress (equation (8)). In a dilute gas, this contribution is usually small compared with the kinetic part since collisions are rare. In contrast, the shear viscosities are typically dominated by the kinetic part of the stress in dilute gases, and essentially independent of the density, consistent with our findings (Figs. 1f–h and 2e and Supplementary Fig. S8).

Comparing the linear response of chiral active fluids with opposite Ω, we find that (up to numerical uncertainty) η^{o}, η^{A} and η^{B} are

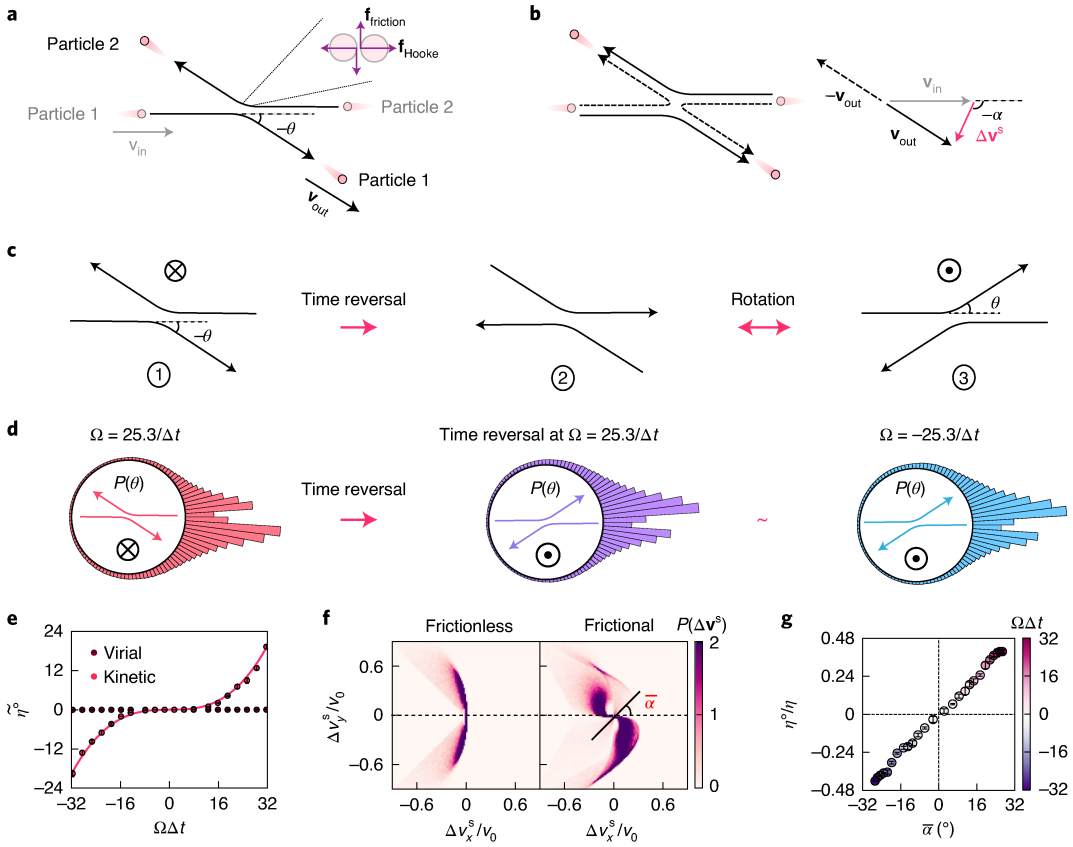

Fig. 2 | Parity-violating collisions and microscopic origin of odd viscosity. Transport coefficients of our dilute granular gas such as its viscosity are mainly determined by the two-particle collision kernel. **a**, Consider a collision between two particles 1 and 2. In the centre-of-mass reference frame, they have incoming velocities $\pm\mathbf{v}_{in}$ and outgoing velocities $\pm\mathbf{v}_{out}$. The scattering angle is defined as $\theta = \text{angle}(\mathbf{v}_{in}, \mathbf{v}_{out})$. **b**, As the particles are identical, we can always assume that $\pm\mathbf{v}_{in}\cdot\pm\mathbf{v}_{out} \geq 0$. We then introduce the velocity change $\Delta\mathbf{v}^s = \mathbf{v}_{out} - \mathbf{v}_{in}$ and the angle $\alpha = \text{angle}(\mathbf{v}_{in}, \Delta\mathbf{v}^s)$, which are directly related to the momentum exchanged between the particles during the collision. **c**, The non-central interaction between two active spinners with surface friction breaks the symmetry between θ and $-\theta$ (see also Supplementary Video S1), or equivalently between α and $-\alpha$. For positive (negative) self-spinning speeds, the particle coming from the left turns slightly downward (upward). In other words, the collisions are chiral. This can be seen by comparing a given collision (①) with the time-reversed collision ($\mathbf{v}\to-\mathbf{v}$, see ②). We can use isotropy to fix the direction of $\mathbf{v}_{in}$. The rotated time-reversed collision ③ differs from the original one ①. **d**. This is quantitatively measured by the scattering angle distributions $P(\theta)$. The scattering angle distribution at self-spinning speed Ω_0 is therefore different from the distribution at $-\Omega_0$. However, it is identical to the time reverse of the angle distributions at $-\Omega_0$. This suggests that, at steady state, the time-reversed dynamics is statistically equivalent to the dynamics with reversed self-spinning speed. **e**, Contribution of the virial and kinetic stresses to odd viscosity η^o (equation (7)). The kinetic part dominates in our dilute granular gas. The number density is $nd^2 = 0.254$. **f**, Distribution of the symmetrized velocity change $P(\Delta\mathbf{v}^s)$. When the particles are frictionless ($\mathbf{f}_{ij}^{nc}$ set to zero), collisions do not break parity. When the particles are frictional, the collisions are chiral and $P(\Delta\mathbf{v}^s)$ displays a chiral distortion with a characteristic twisting angle $\overline{\alpha}$ defined as the average of the angle α in **b**. This twisting angle gives a measure of the parity-violating nature of the collisions. **g**, The odd viscosity ratio η^o/η is proportional to the twisting angle $\overline{\alpha}$. (A similar direct quantitative relation does not exist for the average scattering angle.) Error bars denote standard errors.

odd functions of Ω while η, ζ and η^R are even functions (Fig. 1f–h). Moreover, $\eta^A(\Omega) \approx -\eta^B(-\Omega)$ (Fig. 1g,h). These relations imply (but are not equivalent to) $\eta_{abcd}(\Omega) = \eta_{dcba}(-\Omega)$. These results are reminiscent of Onsager–Casimir reciprocity relations that would occur in an equilibrium fluid[37,38]. The existence of these relations can be understood from the statistical properties of interparticle collision and symmetry considerations (Supplementary Sect. VI). First, the breaking of parity is parameterized by Ω. The system at $-\Omega$ is equivalent to the one at Ω under a mirror reflection $P_x = \text{diag}(-1, 1)$, which changes the sign of the parity-violating viscosities including η^A, η^B and η^o but does not affect the remaining viscosities. Second, although each individual collision is not time-reversal invariant, the time-reversed collisions at Ω are on average equivalent to the collisions at $-\Omega$ (Fig. 2d). This indicates that, near steady state, there is a correspondence between the time-reversed dynamics at Ω and the time-forward dynamics at $-\Omega$, in the statistical sense. From this, we can show that the relations $\eta_{abcd}(\Omega) = \eta_{dcba}(-\Omega)$ hold (Supplementary Sect. VI).

We also find that odd viscosity follows the relation $\eta^o \sim T_{\text{eff}}(\Omega)\,\Omega$ (Fig. 1f), while the shear viscosity $\eta(T_{\text{eff}})$ depends on Ω only through the effective temperature (Supplementary Fig. S6). In Extended Fig. E4, we present the results of large-scale molecular dynamics simulations of a non-linear compression shock: the transverse macroscopic flow induced by odd stress and odd viscosity is directly visible (Supplementary Video S8). Quantitative comparison between numerics and theory corroborates our hydrodynamic description of this chiral active fluid (see also Supplementary Figs. S9–S11).

Fluctuating hydrodynamics

We now turn to the fluctuating hydrodynamics of the chiral active fluid. Standard fluid mechanics is deterministic. However, fluctuations of the hydrodynamic variables must be taken into account

in situations such as the onset of phase transitions and hydrodynamic instabilities, and in turbulent flows. They also determine the correlation functions of the fluid, which in turn control physical properties such as light scattering[39,40]. To describe these fluctuations, let us go back to the Navier–Stokes equation (5) and add to the stress tensor $\boldsymbol{\sigma}$ a fluctuating component $\boldsymbol{\sigma}^{\mathrm{R}}$ with zero mean in addition to the steady-state and viscous components in equation (6). In our chiral active fluid, we find that the correlations of the random stress are of the form

$$\langle \sigma_\alpha^{\mathrm{R}}(\mathbf{r},t)\,\sigma_\beta^{\mathrm{R}}(0,0)\rangle = 2k_{\mathrm{B}}T_{\mathrm{eff}}\,\delta(\mathbf{r})\left[\eta_{\alpha\beta}^{\mathrm{sym}}\delta(t)+\eta_{\alpha\beta}^{\mathrm{anti}}\,\xi(t)\right] \quad (9)$$

in which $\eta_{\alpha\beta}^{\mathrm{sym(anti)}}$ is the symmetric (anti-symmetric) part of the matrix η under index exchange $\alpha\leftrightarrow\beta$, $\delta(t)=\delta(-t)$ is a symmetric function of time peaked at $t=0$ and $\xi(t)=-\xi(-t)$ is an anti-symmetric function peaked near $t=0^{\pm}$ (Supplementary Sect. VI), and $\langle\,\rangle$ denotes an ensemble average at steady state. In standard fluctuating hydrodynamics[39,ch. IX], only the term proportional to $\delta(t)$ is included. Here, the second term has to be added to account for the effect of broken time-reversal invariance. The precise form of the functions $\delta(t)$ and $\xi(t)$ depends on the microscopic model. As shown in Fig. 3a,b and Supplementary Sect. VI, the breaking of time-reversal invariance leads to qualitative changes in the stress correlations computed from molecular dynamics simulations: the imaginary parts of the correlation function in Fig. 3a would vanish identically in a time-reversal invariant system.

Experimentally, it is easier to access the velocity correlation functions

$$c_{ab}(\mathbf{r},t) = \langle u_a(\mathbf{r},t)u_b(0,0)\rangle \quad (10)$$

than the stress correlation functions. The Green's function of the (linearized) Navier–Stokes equation (5) allows us to compute the velocity correlations in equation (10) from the stress correlations in equation (9) (Supplementary Sect. VI). In Fig. 3c–f and Extended Fig. E5, we compare the correlation functions obtained directly from the simulations with our theoretical predictions. In the hydrodynamic regime (wavevector $k\to 0$), there is excellent agreement even when we assume no further information on the fluid than its viscosity coefficients. This corresponds to taking δ to the limit of a Dirac distribution (and similarly for ξ) in equation (9) (Fig. 3e, black curve). A discrepancy occurs at higher wavevectors, in which the microscopic time and length scales contained in the noise become relevant. Good agreement between equation (10) and the simulation results is recovered by using the measured stress correlations (Fig. 3d and red curve in Fig. 3e).

Green–Kubo relations

At equilibrium, correlation functions of the fluctuating stress yield the viscosities of a fluid. This relation, known as the Green–Kubo formula, is a manifestation of the fluctuation–dissipation theorem, whose validity is not guaranteed out of equilibrium[18,19,41–47].

Can the Green–Kubo relations survive in our active fluids? The answer is, in fact, already contained in the fluctuating hydrodynamic theory in equations (5)–(9). The Green–Kubo relations

$$\eta_{\alpha\beta} = \frac{A}{k_{\mathrm{B}}T_{\mathrm{eff}}}\int_0^\infty \langle \sigma_\alpha^{\mathrm{R}}(t)\sigma_\beta^{\mathrm{R}}(0)\rangle\,\mathrm{d}t \quad (11)$$

can be derived by integrating equations (5)–(9) over space and time (A is the area of the 2D system). The second term on the right-hand side of equation (9), which is an anti-symmetric function of time, yields the anti-symmetric part of the viscosity matrix $\eta_{\alpha\beta}$ (containing, for example, the odd viscosity η^{o}). We numerically evaluate the right-hand side of equation (11), focusing on the two fluctuating shear stresses $s_1=\oplus$ and $s_2=\otimes$ (Fig. 4), and compare it with the viscosities obtained from the linear response to finite perturbations. The auto-correlation function $\langle s_1(t)s_1(0)\rangle=\langle s_2(t)s_2(0)\rangle$ yields the shear viscosity η while the cross-correlation function $\langle s_1(t)s_2(0)\rangle=-\langle s_2(t)s_1(0)\rangle$ yields the odd viscosity η^{o} (Fig. 4a). The latter relation manifestly shows that $\eta^{\mathrm{o}}\neq 0$ violates time-reversal symmetry. As shown in Fig. 4b, the values of η and η^{o} computed from the Green–Kubo formula agree well with the values we obtained using the direct hydrodynamic measurements reported in Fig. 1. We verified that the long-time tails associated with the breakdown of 2D hydrodynamics are too small to impact the viscosity prediction (Supplementary Fig. S12).

In Supplementary Sect. VI, we derive both the fluctuating hydrodynamic equations (5)–(9) and the Green–Kubo relations (11) from first principles, without invoking the Onsager regression hypothesis assumed in previous studies[29,48]. By extending the Mori–Zwanzig projection operator formalism[49] to handle the presence of dissipative interactions, we derive the Green–Kubo relation and pinpoint the conditions of its validity. We show that an equilibrium-like Green–Kubo relation for the shear viscosity tensor holds near the steady state of any isotropic active fluid satisfying the following three conditions: (i) the activated and fluctuating degrees of freedom are statistically decoupled, (ii) the steady state is stable under small perturbations and (iii) the ensemble-averaged (microscopic) velocity–velocity correlations $c_{\mathbf{vv}}(\mathbf{r})=\langle\mathbf{v}(0)\cdot\mathbf{v}(\mathbf{r})\rangle$ (Supplementary Figs. S13 and S14) decay faster than r^{-D} (where D is the dimension of the system).

In order to take into account correlations between the particle velocities (see Methods), the normalization factor $k_{\mathrm{B}}T_{\mathrm{eff}}$ in equations (9) and (11) should in general be replaced with

$$k_{\mathrm{B}}T_{\mathrm{eff}}^{*} = k_{\mathrm{B}}T_{\mathrm{eff}} + \rho\,\hat{c}_{\mathbf{vv}}(\mathbf{k}\to 0)/D. \quad (12)$$

For our chiral active fluids with a contact frictional interaction, $c_{\mathbf{vv}}(\mathbf{r})$ is both small and local, causing a small but detectable correction that matches our predictions (Fig. 4b, red line). In wet active fluids, additional modifications of the Green–Kubo relation (11) are required because the hydrodynamic interactions can be non-reciprocal (Supplementary Sect. VI).

Stress fluctuations and rheology

The behaviour of the spatially averaged fluctuating shear stresses of a chiral active fluid can be understood visually from the following observation: the random trajectories of the collective variables $\langle\oplus\rangle_{\mathrm{r}}$ and $\langle\otimes\rangle_{\mathrm{r}}$ in shear–stress space plotted in Fig. 4c are random, confined and have a tendency towards rotation (Supplementary Video S9). Here, $\langle\,\rangle_{\mathrm{r}}$ is an instantaneous spatial average (not the ensemble average $\langle\,\rangle$). To account for these properties, we introduce a minimal model based on the following Langevin equation (see discussions in Supplementary Sect. VII and Fig. S18): where w_1 and w_2 are two independent white noise components, the prefactors $C_\eta = \langle\langle\oplus\rangle_{\mathrm{r}}^2(0)\rangle\cdot A/k_{\mathrm{B}}T_{\mathrm{eff}}^{*}$ and $C_{\mathbf{R}} = \langle\langle\oplus\rangle_{\mathrm{r}}^2(0)\rangle\cdot\sqrt{A/k_{\mathrm{B}}T_{\mathrm{eff}}^{*}\cdot\eta/(\eta^2+\eta^{\mathrm{o}2})}$. When the odd viscosity η^{o} vanishes, equation (13) simply describes the evolution of an overdamped random walker with Cartesian coordinates $(\langle\oplus\rangle_{\mathrm{r}},\langle\otimes\rangle_{\mathrm{r}})$ moving in a harmonic trap. In the presence of a non-vanishing η^{o}, the random walker experiences an additional azimuthal force proportional to its distance from the origin that makes it rotate as shown in Fig. 4c. (This is formally equivalent to the odd elastic springs of ref. [23] with addition of a random noise.) This chiral motion again shows the breaking of time-reversal symmetry caused by η^{o}.

$$\begin{pmatrix}\dot{\langle\oplus\rangle}_{\mathrm{r}}\\ \dot{\langle\otimes\rangle}_{\mathrm{r}}\end{pmatrix} = -C_\eta\begin{pmatrix}\eta & \eta^{\mathrm{o}}\\ -\eta^{\mathrm{o}} & \eta\end{pmatrix}^{-1}\begin{pmatrix}\langle\oplus\rangle_{\mathrm{r}}\\ \langle\otimes\rangle_{\mathrm{r}}\end{pmatrix} + C_{\mathbf{R}}\begin{pmatrix}w_1\\ w_2\end{pmatrix}, \quad (13)$$

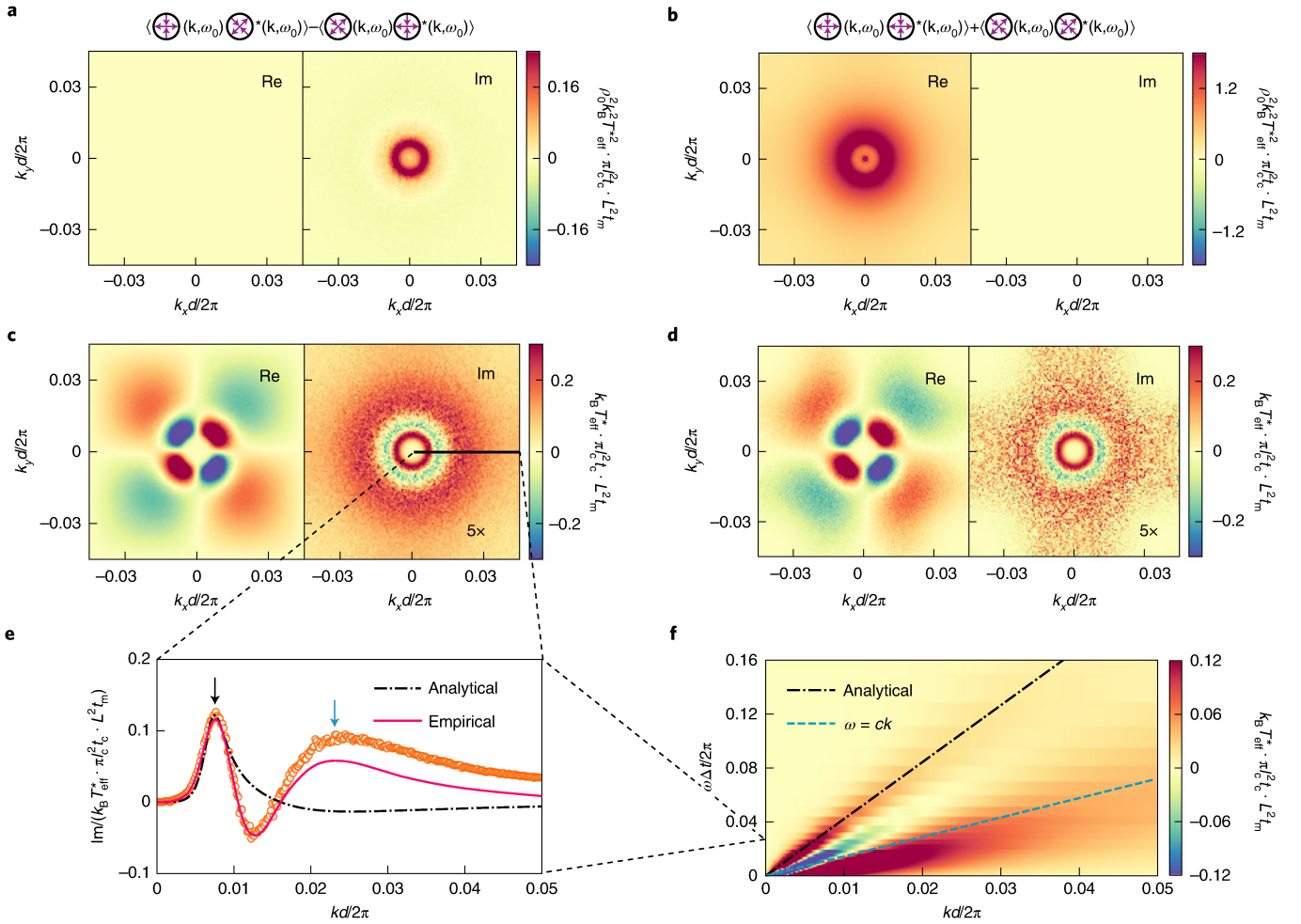

Fig. 3 | Fluctuating hydrodynamics of chiral active fluids. Stress–stress and velocity–velocity correlations obtained from direct measurements in molecular dynamics simulations, compared with the predictions of the fluctuating hydrodynamic theory, as well as the excitation spectrum of the system as a function of frequency ω and wave mode $k=|\mathbf{k}|$. **a**,**b**, Stress–stress correlation functions. The purely imaginary combination $2\mathrm{i}\mathrm{Im}\langle s_1 s_2^*\rangle$ (**a**) is anti-symmetric under time reversal (TR) and is associated with odd viscosity η^o. The purely real component $\langle s_1 s_1^*\rangle + \langle s_2 s_2^*\rangle$ (**b**) is TR symmetric and is associated with shear viscosity η. **c**,**d**, Velocity–velocity correlation functions, comparing the correlation function $c_{xy}(\mathbf{k},\omega) = \langle u_x(\mathbf{k},\omega) u_y^*(\mathbf{k},\omega)\rangle$ measured in particle-based simulation (**c**) with that predicted using our fluctuating hydrodynamic theory (**d**) using the measured stress–stress correlations in **a**,**b**. The real part corresponds to the effects of η, whereas the imaginary part corresponds to η^o. In **c** and **d**, the imaginary parts are magnified five times for readability. **e**, The radially averaged velocity correlation function $\mathrm{Im}\,[c_{xy}(k,\omega)]$, comparing the simulation data (orange points) with (i) an analytical solution (black dashed line) obtained from the linearized fluctuating hydrodynamic theory in which all time scales in the stress correlations are neglected by replacing $\delta(t)$ in equation (9) with a Dirac distribution (and similarly for ξ) and (ii) an empirical solution (red solid line) obtained from the measured momentum-dependent viscosity and stress–stress correlation functions (Supplementary Figs. S16 and S17). The simplified analytical solution (i) assumes a constant viscosity tensor and applies only in the hydrodynamic limit: it indeed captures the first peak at $k_1 = 0.015\pi/d$ of the velocity correlation function in **e**. The empirical estimation (ii) also captures the second peak at $k_2 = 0.047\pi/d$, which was completely missed by the linear theory. The first and second peaks are marked with black and blue arrows, respectively. **a**–**e** correspond to a fixed excitation (wave) frequency $\omega = \omega_0 \equiv 0.055\pi/\Delta t$ (but different wavevectors $\mathbf{k}$). **f**, Power spectrum of $\mathrm{Im}[c_{xy}(k,\omega)]$. Our theoretical prediction on the position of the first peak (black dashed line) applies to a wide range of frequencies ω. We also find that the second peak is associated with the dispersion relation of the fluid $\omega = ck$ (cyan dashed line).

In Supplementary Sect. VII, we solve equation (13) analytically and find closed-form expressions for the stress–stress correlation functions (Fig. 4a, continuous lines) that match well with the molecular dynamics simulation measurements (Fig. 4a, dots). By Fourier transforming these analytically derived correlation functions, we can predict the viscous response to an oscillatory shear with frequency f. The complex shear viscosity $\eta(f) = \eta'(f) - \mathrm{i}\,\eta''(f)$ is related to the dynamic (complex) shear modulus $G(f) = G'(f) + \mathrm{i}\,G''(f)$ through $\eta' = G''/[2\pi f]$ and $\eta'' = G'/[2\pi f]$ (ref. [50]). Here, G' is the storage modulus describing the elastic response and G'' is the loss modulus describing the viscous response. Similarly, a complex odd viscosity $\eta^o(f) = \eta^{o\prime}(f) - \mathrm{i}\,\eta^{o\prime\prime}(f)$ can be related to an odd dynamic modulus $G^o(f) = \eta^o(f)/[2\pi\mathrm{i}f]$. See also ref. [51] for a discussion of odd viscoelastic materials. As illustrated in Fig. 4d,e, the predicted $\eta(f)$ and $\eta^o(f)$ are in excellent agreement with numerical data. This provides a finite-frequency extension of the Green–Kubo formula.

Statistical decoupling and mutual information

Is the presence of an equilibrium-like Green–Kubo relation restricted to chiral active fluids? To investigate this question, we performed extensive simulations of active Brownian rollers and oscillating granular gases (Fig. 5). In both cases, the non-equilibrium

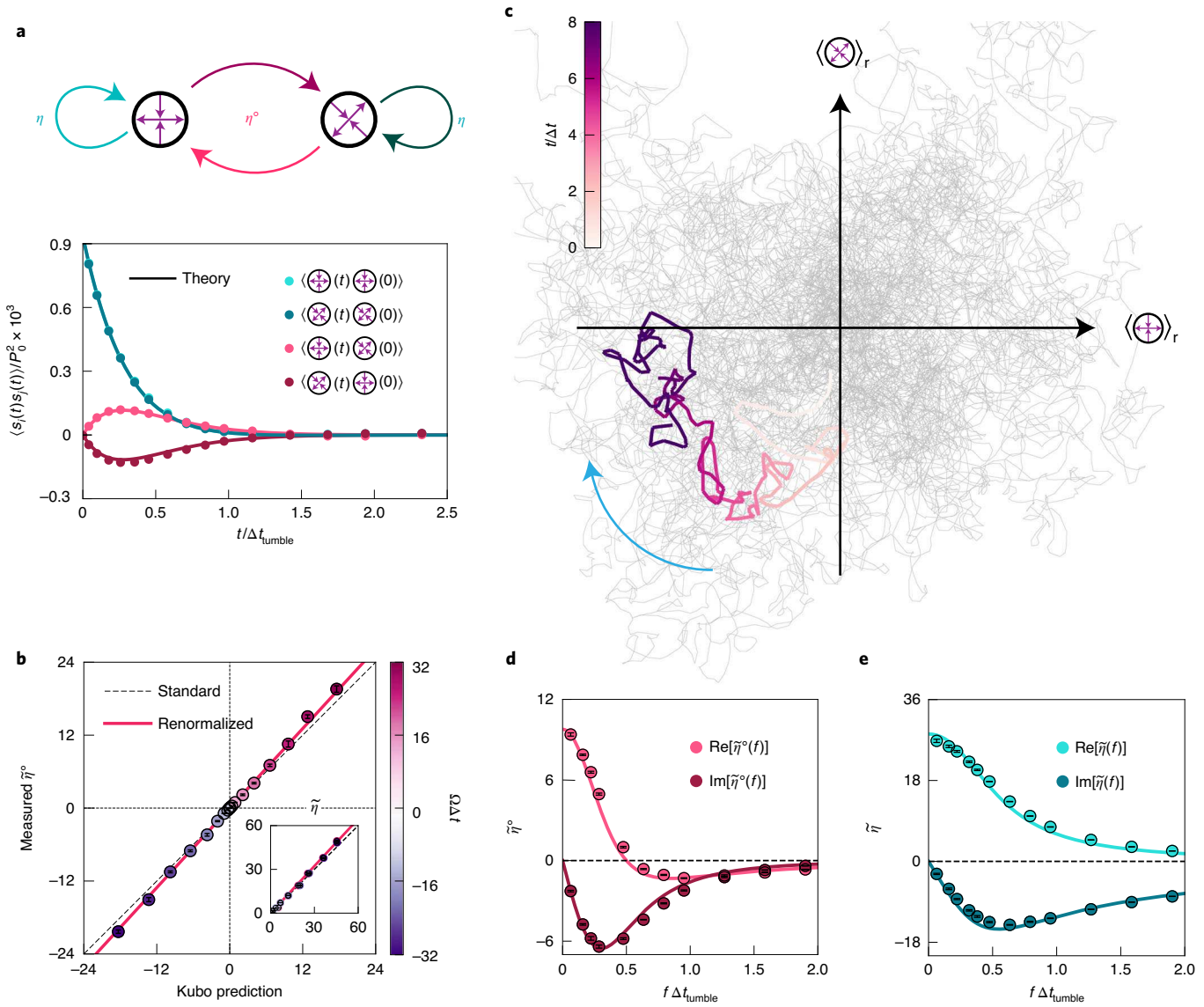

Fig. 4 | Green–Kubo relations and rheology in chiral active fluids. a, Stress–stress correlation functions. The time correlation functions of the two global shear stresses $\langle\oplus\rangle_r$ and $\langle\otimes\rangle_r$ are plotted. The shear viscosity η leads to the auto-correlations (green), whereas the odd viscosity η° gives rise to the cross-correlations (red), as summarized in the top schematic. The correlation functions predicted by our theory using equation (13) are compared with the values measured in simulations. The correlation time is set by the tumbling time of a particle $\Delta t_{\mathrm{tumble}} = (\Delta t + \Delta t_{\mathrm{col}}) \cdot \bar{v}/\overline{\Delta v}$ required for a particle to randomize its direction, where Δt is the collision duration, Δt_{col} is the time between collisions, $\bar{v}$ is the mean velocity of the particle and $\overline{\Delta v}$ is the average velocity change after a collision. We find that $\Delta t_{\mathrm{tumble}} \approx 100\Delta t$ in this case. **b**, Green–Kubo relation. The shear viscosities under constant shear are related to the integrated stress–stress correlations through the so-called direct-current (DC) Green–Kubo relation. The measured odd viscosity η° is compared with the Green–Kubo prediction for a wide range of spinning speeds Ω. Inset: comparison between the predicted and measured shear viscosity η. The Green–Kubo predictions with T_{eff} and the renormalized T^*_{eff} are marked as dashed and solid lines, respectively. **c**, Time evolution of the shear stress vector ($\langle\oplus\rangle_r$, $\langle\otimes\rangle_r$) at spinning speed $\Omega = 25.3/\Delta t$. At steady state of the chiral active fluid, the shear stress vector traces out a 2D random walk in the stress space (grey curve in background), which is loosely confined and rotates around the origin preferentially in a clockwise fashion over time (curve with gradient colouring). **d**,**e**. Green–Kubo relation in frequency domain. The frequency-dependent coefficients of the viscous response to an oscillatory shear with frequency f can be estimated using the Fourier transform of the stress–stress correlation functions. This is the so-called alternating-current (AC) Green–Kubo relation. Comparisons between the Green–Kubo predictions and the simulation measurements are presented for both odd viscosity (**d**) and shear viscosity (**e**) at various shear frequencies f. Error bars denote standard errors.

steady state follows an approximate Boltzmann distribution (Fig. 5e,h), parameterized by an effective temperature T_{eff} controlled by the respective sources of activity. In addition, Fig. 5f,i shows that a Green–Kubo relation also applies to the shear viscosity of oscillating granular gases and the drag coefficient of active Brownian rollers with the same T_{eff} values measured in Fig. 5e,h.

We trace the validity of the Green–Kubo relation in all these systems to the statistical decoupling between activated and fluctuating degrees of freedom. Energy is passed from the environment to the fluctuating degrees of freedom through the activated ones. Yet, the activated and fluctuating degrees of freedom can still be almost statistically independent. This is evidenced by Fig. 6, in which we

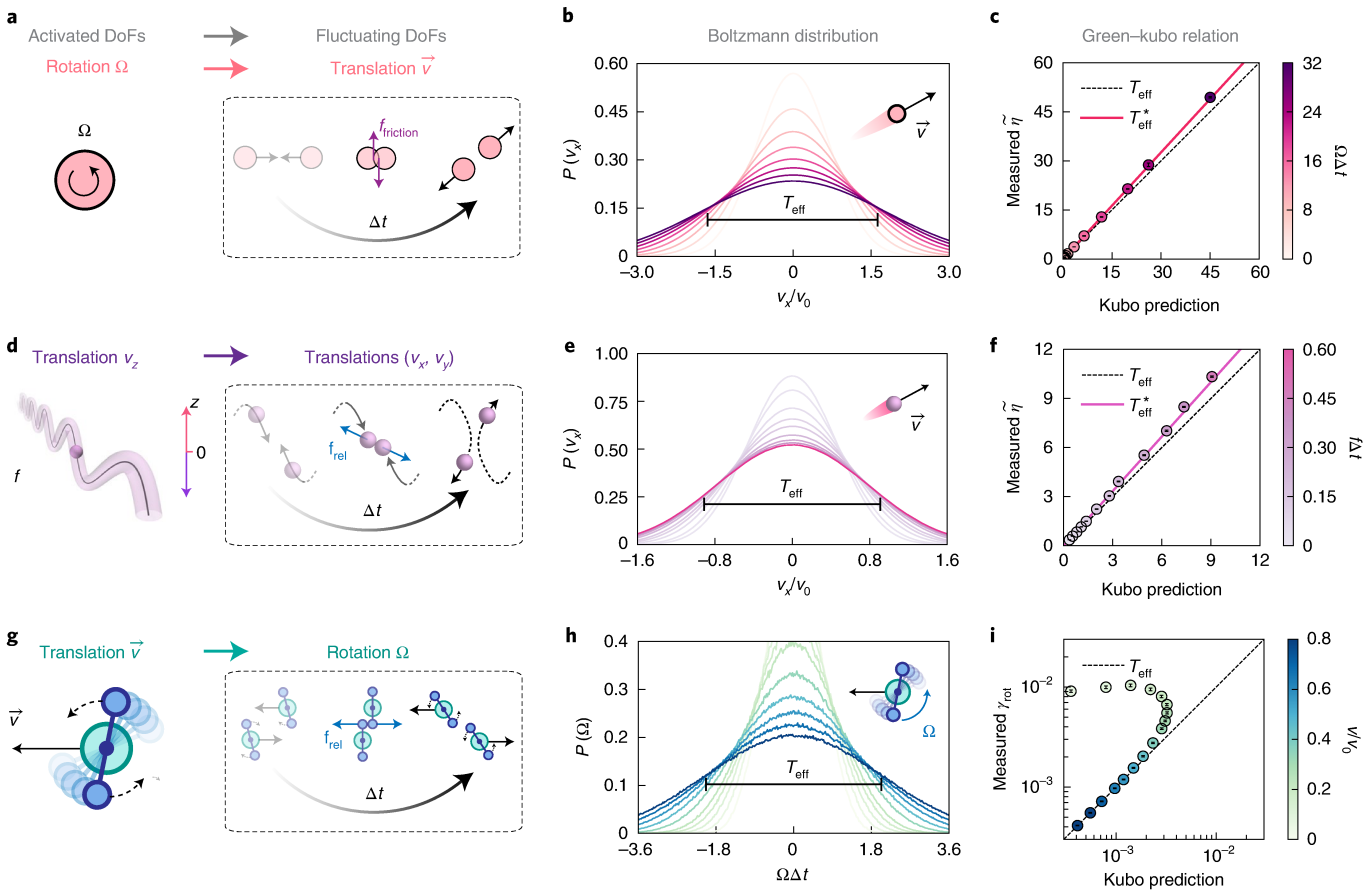

Fig. 5 | Effective thermodynamics in a chiral active fluid, oscillating granular gas and active Brownian rollers. We consider three examples of active fluids in which the degrees of freedom are split into (i) activated degrees of freedom that are directly powered by energy consumption but whose dynamics reduces to a constraint on the relevant time scales and (ii) fluctuating degrees of freedom that are powered through the activated ones (**a**,**d**,**g**). We find that the fluctuating degrees of freedom follow a Boltzmann distribution (**b**,**e**,**h**) and satisfy a Green–Kubo relation (**c**,**f**,**i**) when they are statistically decoupled from the activated degrees of freedom (Fig. 6). **a**–**c**. Chiral active fluid. In this system, the active rotation of the particles powers their translational motion during collisions. The induced translational velocity displays a Boltzmann distribution parameterized by an effective temperature $T_{\rm eff} = m\langle v_x^2\rangle/k_{\rm B}$. The shear viscosity η satisfies the Green–Kubo relation associated with a renormalized temperature $T^*_{\rm eff}$, which quantifies the collective velocity fluctuations of a particle with its neighbours. **d**–**f**, Active oscillators. The particles oscillate in the z-direction at a constant frequency f with random initial phases. During collision, their vertical oscillation causes translations in the x–y plane. This induced horizontal translation displays a Boltzmann distribution as well as a Green–Kubo relation. See Extended Fig. E1 for more details. **g**–**i**, Active Brownian rollers. Active Brownian particles (green) hinged with a dumbbell (blue) self-propel at a constant speed v. During collision, this active translation causes a random rotation of the dumbbells, the angular velocity $\boldsymbol{\Omega}$ of which follows a Boltzmann distribution. The rotational drag coefficient $\gamma_{\rm rot}$ measured via the linear response follows a Green–Kubo relation at high activity v but exhibits significant deviations from the Green–Kubo value at low activity v (**i**). The damping coefficient $\gamma_{\rm rot}$ characterizes the relaxation of the rotation of individual particles (unlike the shear viscosity η that describes the relaxation of collective hydrodynamic variables). Hence, the effective temperature $T_{\rm eff} = I\langle\Omega^2\rangle/2k_{\rm B}$ (where I is the moment of inertia) entering the Green–Kubo relation includes no correction from correlations (contrary to the two other systems in which the renormalized temperature $T^*_{\rm eff}$ appears). See Extended Fig. E2 for more details. We define $v_0 = d/\Delta t$. The number density is $nd^2 = 0.254$ in both the chiral active fluid and oscillating granular gas, whereas $nd^2 = 0.076$ in the system of active Brownian rollers. Error bars denote standard errors.

plot the mutual information between the activated and fluctuating degrees of freedom, defined as the Kullback–Leibler divergence[52]

$$I^{(\mathrm{a,f})} = \int P(X^{\mathrm{a}}, X^{\mathrm{f}}) \ln\left[\frac{P(X^{\mathrm{a}}, X^{\mathrm{f}})}{P(X^{\mathrm{a}})\,P(X^{\mathrm{f}})}\right] \mathrm{d}X^{\mathrm{a}}\mathrm{d}X^{\mathrm{f}} \qquad (14)$$

between the post-collision joint distribution of the random variables X^{a} and X^{f} associated with the activated and fluctuating degrees of freedom and the products of their marginal distributions (Supplementary Sect. VIII). To allow comparison between different systems, we normalize the mutual information $I^{(\mathrm{a,f})}$ by the joint entropy $H^{(\mathrm{a,f})}$ between X^{a} and X^{f}. The factorization of the joint distributions (or lack thereof) is illustrated in Fig. 6. Crucially, the deviation from the Green–Kubo relation for active Brownian rollers in Fig. 6j coincides with a sharp increase of the mutual information. The Green–Kubo formula for the fluctuating rotational degrees of freedom is valid in the limit of large self-propulsion speed (or high drag coefficient; see Extended Fig. E2c and d, respectively), where the drive wipes out most correlations with the activated translational degrees of freedom. In contrast, the mutual information is approximately constant in Fig. 6b,f. Here, the Green–Kubo relation is always valid for the range of parameters we explored.

Our fluctuating hydrodynamic theory of active fluids offers a probe of their anomalous transport coefficients and paves the way for studies of chiral active turbulence.

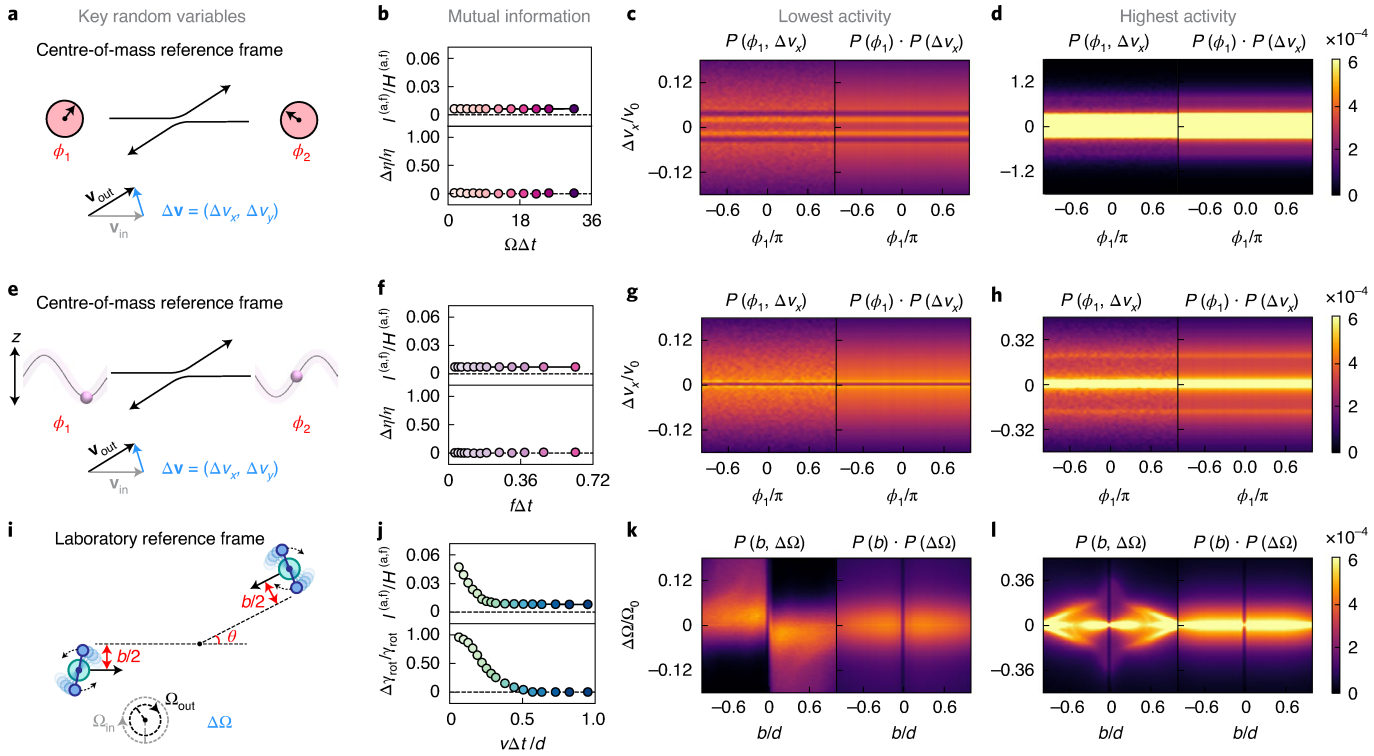

Fig. 6 | Mutual information in a chiral active fluid, oscillating granular gas and active Brownian rollers. We quantify the statistical interdependence between the activated and fluctuating degrees of freedom (DoFs) during collision by computing the mutual information $I^{(a,f)}$ (defined in equation (14)) between them. We first identify the key random variables for the activated and fluctuating DoFs during collision, which are marked in red and blue, respectively, in **a**,**e**,**i**. By performing simulations of scattering events, we then sample the joint probability distributions of those random variables, which allows us to further calculate $I^{(a,f)}$. In **b**,**f**,**j**, we compare the mutual information $I^{(a,f)}$ normalized by the joint entropy $H^{(a,f)}$ and the deviation from the Green–Kubo relation for a wide range of activity. **a**–**d**. Chiral active fluid. We select the initial orientation of the two spinners (ϕ_1, ϕ_2) as the random variables for active rotations, and the velocity change upon collision $\Delta\mathbf{v} = (\Delta v_x, \Delta v_y)$ as the random variable for fluctuating translations (**a**). Due to the isotropic nature of the spinners, the collision should not depend on particle orientations. Indeed, the normalized mutual information $I^{(a,f)}/H^{(a,f)}$ between (ϕ_1, ϕ_2) and $(\Delta v_x, \Delta v_y)$ is negligible, suggesting that the activated and fluctuating DoFs are statistically decoupled (**b**). The small, non-zero residue in $I^{(a,f)}/H^{(a,f)}$ is caused by the noise in the probability distribution sampled from simulations. Consistently, the relative difference between the measured shear viscosity and the Kubo prediction, $\Delta\eta/\eta = (\eta - \eta_{Kubo})/\eta$, is negligible. To further demonstrate the statistical independence, we plot the joint distribution $P(\phi_1, \Delta v_x)$ (**c**) and the products of marginal distributions $P(\phi_1)P(\Delta v_x)$ (**d**) at both the lowest and highest activities (first and last points in **b**). The results show that the probability distribution of the activated and fluctuating DoFs can indeed be factorized. **e**–**h**. Active oscillators. Selecting the initial phases of the two oscillators (ϕ_1, ϕ_2) and the velocity change $\Delta\mathbf{v} = (\Delta v_x, \Delta v_y)$ as the key random variables, these results show that these activated and fluctuating DoFs are also statistically decoupled. **i**–**l**. Active Brownian rollers. We select the impact parameter b and the incident angle θ as the random variables for active translations and the change in the rotation velocity $\Delta\Omega$ as the key random variable for the linear response in fluctuating rotations. The normalized mutual information $I^{(a,f)}/H^{(a,f)}$ and the deviation from the Kubo relation quantified as $\Delta\gamma_{rot}/\gamma_{rot} = (\gamma_{rot} - \gamma_{rot\text{-}Kubo})/\gamma_{rot}$ simultaneously decrease with activity (**j**).

Online content

Any methods, additional references, Nature Research reporting summaries, source data, extended data, supplementary information, acknowledgements, peer review information; details of author contributions and competing interests; and statements of data and code availability are available at https://doi.org/10.1038/s41567-021-01360-7.

Received: 17 April 2020; Accepted: 16 August 2021;
Published online: 8 November 2021

References

1. Kadanoff, L. P. Built upon sand: theoretical ideas inspired by granular flows. *Rev. Mod. Phys.* **71**, 435–444 (1999).
2. de Gennes, P. G. Granular matter: a tentative view. *Rev. Mod. Phys.* **71**, S374–S382 (1999).
3. Jaeger, H. M., Nagel, S. R. & Behringer, R. P. Granular solids, liquids, and gases. *Rev. Mod. Phys.* **68**, 1259–1273 (1996).
4. Grzybowski, B. A., Stone, H. A. & Whitesides, G. M. Dynamic self-assembly of magnetized, millimetre-sized objects rotating at a liquid–air interface. *Nature* **405**, 1033–1036 (2000).
5. Tsai, J.-C., Ye, F., Rodriguez, J., Gollub, J. P. & Lubensky, T. A chiral granular gas. *Phys. Rev. Lett.* **94**, 214301 (2005).
6. Fürthauer, S., Strempel, M., Grill, S. W. & Jülicher, F. Active chiral fluids. *Eur. Phys.* **35**, 1–13 (2012).
7. Nguyen, N. H., Klotsa, D., Engel, M. & Glotzer, S. C. Emergent collective phenomena in a mixture of hard shapes through active rotation. *Phys. Rev. Lett.* **112**, 075701 (2014).
8. van Zuiden, B. C., Paulose, J., Irvine, W. T. M., Bartolo, D. & Vitelli, V. Spatiotemporal order and emergent edge currents in active spinner materials. *Proc. Natl Acad. Sci. USA* **113**, 12919–12924 (2016).
9. Banerjee, D., Souslov, A., Abanov, A. G. & Vitelli, V. Odd viscosity in chiral active fluids. *Nat. Commun.* **8**, 1573 (2017).
10. Scholz, C., Engel, M. & Pöschel, T. Rotating robots move collectively and self-organize. *Nat. Commun.* **9**, 931 (2018).
11. Soni, V. et al. The odd free surface flows of a colloidal chiral fluid. *Nat. Phys.* **15**, 1188–1194 (2019).
12. Yeo, K., Lushi, E. & Vlahovska, P. M. Collective dynamics in a binary mixture of hydrodynamically coupled microrotors. *Phys. Rev. Lett.* **114**, 188301 (2015).

13. Markovich, T., Tjhung, E. & Cates, M. E. Chiral active matter: microscopic 'torque dipoles' have more than one hydrodynamic description. *New J. Phys.* **21**, 112001 (2019).
14. Oppenheimer, N., Stein, D. B. & Shelley, M. J. Rotating membrane inclusions crystallize through hydrodynamic and steric interactions. *Phys. Rev. Lett.* **123**, 148101 (2019).
15. Riedel, I. H., Kruse, K. & Howard, J. A self-organized vortex array of hydrodynamically entrained sperm cells. *Science* **309**, 300–303 (2005).
16. Petroff, A. P., Wu, X.-L. & Libchaber, A. Fast-moving bacteria self-organize into active two-dimensional crystals of rotating cells. *Phys. Rev. Lett.* **114**, 158102 (2015).
17. Rouyer, F. & Menon, N. Velocity fluctuations in a homogeneous 2D granular gas in steady state. *Phys. Rev. Lett.* **85**, 3676–3679 (2000).
18. D'Anna, G., Mayor, P., Barrat, A., Loreto, V. & Nori, F. Observing Brownian motion in vibration-fluidized granular matter. *Nature* **424**, 909–912 (2003).
19. Ojha, R., Lemieux, P.-A., Dixon, P., Liu, A. & Durian, D. Statistical mechanics of a gas-fluidized particle. *Nature* **427**, 521 (2004).
20. Romanczuk, P., Bär, M., Ebeling, W., Lindner, B. & Schimansky-Geier, L. Active Brownian particles. *Eur. Phys. J.: Spec. Top.* **202**, 1–162 (2012).
21. Cates, M. E. & Tailleur, J. Motility-induced phase separation. *Annu. Rev. Condens. Matter Phys.* **6**, 219–244 (2015).
22. Luding, S. Cohesive, frictional powders: contact models for tension. *Granul. Matter* **10**, 235–246 (2008).
23. Scheibner, C. et al. Odd elasticity. *Nat. Phys.* **16**, 475–480 (2020).
24. Avron, J. Odd viscosity. *J. Stat. Phys.* **92**, 543–557 (1998).
25. Irving, J. & Kirkwood, J. G. The statistical mechanical theory of transport processes. IV. the equations of hydrodynamics. *J. Chem. Phys.* **18**, 817–829 (1950).
26. Condiff, D. W. & Dahler, J. S. Fluid mechanical aspects of antisymmetric stress. *Phys. Fluids* **7**, 842 (1964).
27. Evans, D. J. & Morriss, G. *Statistical Mechanics of Nonequilibrium Liquids* (Cambridge Univ. Press, 2008).
28. Souslov, A., Dasbiswas, K., Fruchart, M., Vaikuntanathan, S. & Vitelli, V. Topological waves in fluids with odd viscosity. *Phys. Rev. Lett.* **122**, 128001 (2019).
29. Epstein, J. M. & Mandadapu, K. Time reversal symmetry breaking in two-dimensional non-equilibrium viscous fluids. Preprint at https://arxiv.org/abs/1907.10041 (2019).
30. Korving, J., Hulsman, H., Knaap, H. & Beenakker, J. Transverse momentum transport in viscous flow of diatomic gases in a magnetic field. *Phys. Lett.* **21**, 5–7 (1966).
31. Wiegmann, P. & Abanov, A. G. Anomalous hydrodynamics of two-dimensional vortex fluids. *Phys. Rev. Lett.* **113**, 034501 (2014).
32. Markovich, T & Lubensky, T. C. Odd viscosity in active matter: microscopic origin and 3d effects. Preprint at https://arxiv.org/abs/2006.05662 (2020).
33. Berdyugin, A. I. et al. Measuring Hall viscosity of graphene as electron fluid. *Science* **364**, 162–165 (2019).
34. Bradlyn, B., Goldstein, M. & Read, N. Kubo formulas for viscosity: Hall viscosity, Ward identities, and the relation with conductivity. *Phys. Rev. B* **86**, 245309 (2012).
35. Hoyos, C. & Son, D. T. Hall viscosity and electromagnetic response. *Phys. Rev. Lett.* **108**, 066805 (2012).
36. De Groot, S. R. & Mazur, P. *Non-equilibrium Thermodynamics* (Courier Corporation, 2013).
37. Casimir, H. B. G. On Onsager's principle of microscopic reversibility. *Rev. Mod. Phys.* **17**, 343 (1945).
38. Geigenmüller, U., Titulaer, U. & Felderhof, B. The approximate nature of the Onsager–Casimir reciprocal relations. *Phys. A* **119**, 53–66 (1983).
39. Landau, L. et al. *Statistical Physics, Part 2: Theory of the Condensed State, Course of Theoretical Physics*, Vol. 9 (Elsevier Science, 1980).
40. de Zarate, J. M. O. & Sengers, J. V. *Hydrodynamic Fluctuations in Fluids and Fluid Mixtures* (Elsevier, 2006).
41. Kurchan, J. In and out of equilibrium. *Nature* **433**, 222–225 (2005).
42. Ciliberto, S., Joubaud, S. & Petrosyan, A. Fluctuations in out-of-equilibrium systems: from theory to experiment. *Theory Exp.* **2010**, P12003 (2010).
43. Cugliandolo, L. F. The effective temperature. *J. Phys. A* **44**, 483001 (2011).
44. Loi, D., Mossa, S. & Cugliandolo, L. F. Effective temperature of active matter. *Phys. Rev. E* **77**, 051111 (2008).
45. Seifert, U. Stochastic thermodynamics, fluctuation theorems and molecular machines. *Rep. Prog. Phys.* **75**, 126001 (2012).
46. Shokef, Y., Bunin, G. & Levine, D. Fluctuation–dissipation relations in driven dissipative systems. *Phys. Rev. E* **73**, 046132 (2006).
47. Makse, H. A. & Kurchan, J. Testing the thermodynamic approach to granular matter with a numerical model of a decisive experiment. *Nature* **415**, 614–617 (2002).
48. Kubo, R., Yokota, M. & Nakajima, S. Statistical-mechanical theory of irreversible processes. II. Response to thermal disturbance. *J. Phys. Soc. Jpn* **12**, 1203–1211 (1957).
49. Zwanzig, R. *Nonequilibrium Statistical Mechanics*, 3rd edn (Oxford Univ. Press, 2001).
50. Oswald, P. *Rheophysics – The Deformation and Flow of Matter* (Cambridge Univ. Press, 2014).
51. Banerjee, D., Vitelli, V., Jülicher, F. & Surówka, P. Active viscoelasticity of odd materials. *Phys. Rev. Lett.* **126**, 138001 (2021).
52. MacKay, D. J. C. *Information Theory, Inference and Learning Algorithms* (Cambridge Univ. Press, 2003).

Methods

Models and simulations. *Chiral active fluid.* We study the behaviour of a quasi-2D chiral active fluid composed of spinning components[5–7,10,13,16,53–56]. The microscopic model is presented in the main text (equations (1) and (2)). This model is adapted from standard models of frictional granular disks (see ref. [22] as well as the documentation of the LAMMPS package[57,58] (`pair_granular`) and references therein). Compared with these standard granular models[22,57,58], here we make the following simplifications: (i) rolling friction is ignored and (ii) the frictional coefficients in the normal (radial) and tangential directions take the same value γ.

To prevent complete interpenetration between the particles, we add a non-linearity to the repulsion $\mathbf{f}^{c}$, with a distance-dependent Hookean coefficient that diverges at $r_{ij}=0$:

$$k(r_{ij}) = k\left(1+\alpha\frac{d}{r_{ij}}\right). \tag{M.1}$$

Regarding $\mathbf{f}_{ij}^{nc}$ in equation (3), we emphasize that this interaction is not central, and not invariant under spatial transformations that change orientation (such as reflections). Hence, this granular gas is an example of a broader class of systems called parity-violating fluids[9,24,35] that includes driven granular gases[5,8], rotating colloids[11,12,59–61], polyatomic gases in magnetic fields[30], vortex fluids[31] and electronic fluids[33,34].

The model defined by equations (1) and (2) is analysed through particle-based simulations using a customized version of the LAMMPS package[57,58]. We choose the area fraction of the system to be $\phi=0.2$ and set $\gamma_{rot}=3md^2/t_0$, $\gamma=0.015m/t_0$, $k=m/t_0^2$ and $\alpha=0.3$, where m is the particle mass, t_0 is the unit of time of the simulation and d is the unit of length of the simulation. The interaction timescale $\Delta t=\sqrt{m/k}$ is then $\Delta t=t_0$. To focus on the viscous effects emergent from particle interactions, a frictionless background is used. All the simulations are initialized with a random velocity distribution. The results are collected after the system reaches steady state. In Supplementary Sect. I, we detail specific procedures for investigating the effective thermodynamics[41,43,44,59,62–66] (including anti-symmetric stress[26,67–71]), kinetics, linear response, Green–Kubo relation[41,42,45,63,66,72–82] and hydrodynamics.

Active oscillators. Consider a quasi-2D granular gas composed of the same particles as the chiral fluid. Instead of self-spinning, all the particles oscillate in the z direction at a constant frequency f. In particular, each particle is driven to move in the range $z\in[-A,A]$ with a target velocity profile

$$v_0(t) = 2\pi\omega A\sin(\omega t+\phi), \tag{M.2}$$

where $\omega=2\pi f$ is the angular frequency and ϕ is a random initial phase of the oscillation. To ensure that all particles stay roughly in the same horizontal plane ($z=0$), a linear restoring force $\mathbf{f}=-k_z z\,\hat{\mathbf{z}}$ is added. The microscopic dynamics of the system can be summarized as

$$m\ddot{x}_i = \sum_{j\in N(i)} f_{ij,x}, \tag{M.3}$$

$$m\ddot{y}_i = \sum_{j\in N(i)} f_{ij,y}, \tag{M.4}$$

$$m\ddot{z}_i = c_d\left[v_{i,0}(t)-v_{i,z}\right]-k_z z+\sum_{j\in N(i)} f_{ij,z}, \tag{M.5}$$

where c_d is a large drag coefficient that forces the particle velocity $v_{i,z}$ to quickly relax to $v_{i,0}(t)$. The conservative part of the interaction $\mathbf{f}_{ij}^{c}$ is the same as before (see equation (3)). The dissipative interaction here takes the form

$$\mathbf{f}_{ij}^{nc} = \begin{cases} -\gamma\mathbf{v}_{ij}, & r_{ij}<d,\\ 0 & r_{ij}\geq d. \end{cases} \tag{M.6}$$

Upon collision, the z-directional oscillations of the particles induce random motions in the x–y plane.

All the simulations are performed at an area fraction $\phi=0.2$. We set the parameters $A=d$ and $c_d=100m/t_0$ for the oscillation, $\gamma=0.015m/t_0$, $k=m/t_0^2$ and $\alpha=0.3$ for the particle interaction.

To confirm the Boltzmann statistics, we measure the probability distribution of the induced horizontal velocity at various oscillating frequencies $f\in[0.03/\Delta t, 0.6/\Delta t]$. We measure the effective temperature as $T_{eff}=m\langle v_x^2\rangle/k_B$. In addition, we also measure the density profile of the system when exposed to an external potential well of magnitude $-0.5k_BT_{eff}$.

Finally, we study the Green–Kubo relation for the shear viscosity (equation (11) with $\alpha=\beta=2$ or 3, see the following section for the notations) for $f\in[0.03/\Delta t, 0.6/\Delta t]$, by comparing the value directly measured from linear response under shear flow with the Kubo prediction at steady state. The detailed procedure is identical to that described for the chiral active fluid in Supplementary Sect. I.

Active Brownian rollers. Consider a 2D system composed of active Brownian rollers. Each roller contains a core particle of mass m_c and diameter d_c as well as two dumbbell particles of mass m_r and diameter d_r, which are away from the roller centre by s, hinged to the core particle by a rigid bond and free to rotate about it (Extended Fig. E2). The core particle self-propels at a constant speed v in its own orientation $\hat{\mathbf{e}}=(\cos\theta,\sin\theta)$, where θ is the tilt angle of the orientation director against the x axis. The excluded-volume effects of both the core and dumbbell particles are modelled by the conservative interaction $\mathbf{f}_{ij}^{c}$ in equation (3). However, no dissipative interaction is included. During collision, the self-propulsion of two active Brownian rollers could cause random rotation of their dumbbells, which is quantified by the rotation speed Ω. The microscopic dynamics of the system is described as

$$m_c\ddot{\mathbf{x}}_i = c_d\left[v\hat{\mathbf{e}}_i-\mathbf{v}_i\right]+\sum_{j\in N(i)}\mathbf{f}_{ij}+\boldsymbol{\xi}_{\mathbf{x}}(t) \tag{M.7}$$

$$I_c\ddot{\theta}_i = -\Gamma_c\dot{\theta}_i+\xi_\theta(t) \tag{M.8}$$

$$I_r\dot{\Omega}_i = \sum_{j\in N(i)}\boldsymbol{\tau}_{ij} \tag{M.9}$$

where c_d and Γ_c are the translational and rotational drag coefficients for the core particle, $\boldsymbol{\xi}_{\mathbf{x}}(t)$ is the white noise for translational motion satisfying $\langle\xi_{\mathbf{x},a}(t)\xi_{\mathbf{x},b}(t')\rangle=2c_dk_BT_{\mathbf{x}}\delta(t-t')$, $\xi_\theta(t)$ is the white noise for the reorientation of the director $\hat{\mathbf{e}}$ satisfying $\langle\xi_\theta(t)\xi_\theta(t')\rangle=2\Gamma_ck_BT_\theta\delta(t-t')$, and I_c and I_r are the moments of inertia for the core and dumbbell particles, respectively. $\boldsymbol{\tau}_{ij}$ is the total torque exerted on the dumbbell of particle i by particle j, as a consequence of both the core–dumbbell and dumbbell–dumbbell interactions. These interparticle collisions lead to an effective drag coefficient γ_{rot} for the rotation of the dumbbell.

All the simulations are performed at an area fraction $\phi=0.06$. We set the parameters $m_c=m$, $d_c=d$ and $I_c=0.1md^2$ for the core particle, $d_r=0.2d$, $m_r=m$, $I_r=0.728md^2$ and $s=0.6d$ for the dumbbell, $c_d=100m/t_0$ and $k_BT_x=0$ for active translation, $\Gamma_c=c_dd^2$ and $k_BT_\theta=10^{-3}md^2/t_0^2$ for the director reorientation, and finally $k=m/t_0^2$, and $\alpha=0.3$ for particle interactions.

To validate the Boltzmann statistics, we measure the probability distribution of the dumbbell rotation speed Ω at various self-propulsion speed $v\in[0.06d/\Delta t, 0.8d/\Delta t]$. From the measured probability distribution $P(\Omega)$, we can quantify the effective temperature $T_{eff}=I_r\langle\Omega^2\rangle/k_B$.

We also study the Green–Kubo relation of the effective rotational drag coefficient γ_{rot} for a wide range of self-propulsion speed $v\in[0.06d/\Delta t, 0.8d/\Delta t]$ at a constant $c_d=100md/\Delta t$ as well as a wide range of drag coefficient $c_d\in[0.1md/\Delta t, 10^3md/\Delta t]$ at a constant $v=0.3d/\Delta t$. In particular, we directly measure γ_{rot} by investigating the linear response of single-particle rotation towards a small external torque $\tau_{ext}\in[10^{-4}md^2/\Delta t^2, 10^{-3}md^2/\Delta t^2]$, and further compared it with the Kubo prediction

$$\gamma_{rot} = \frac{1}{k_BT_{eff}}\int_0^\infty\langle\tau(t)\tau(0)\rangle\,dt, \tag{M.10}$$

where $\tau(t)$ is the fluctuating random torque experienced by a given particle due to collision with its neighbours at steady state.

Viscosity: notations and symmetry considerations. In this section, we introduce the notation used in equation (6) of the main text and discuss how various physical symmetries restrict the form of the viscosity tensor. The viscous stress tensor is linearly related to velocity gradients by the viscosity tensor through the equation

$$\sigma_{ab}^{vis} = \eta_{abcd}\,\dot{e}_{cd}, \tag{M.11}$$

where σ_{ab}^{vis} is the viscous stress tensor, $\dot{e}_{cd}=\partial_d u_c$ is the (unsymmetrized) velocity gradient tensor and η_{abcd} is the viscosity tensor.

Following refs. [23,24], we introduce the following basis for rank-2 tensors in two dimensions:

$$\tau_{ab}^0=\begin{pmatrix}1&0\\0&1\end{pmatrix}\quad\tau_{ab}^1=\begin{pmatrix}0&-1\\1&0\end{pmatrix}$$
$$\tau_{ab}^2=\begin{pmatrix}1&0\\0&-1\end{pmatrix}\quad\tau_{ab}^3=\begin{pmatrix}0&1\\1&0\end{pmatrix}. \tag{M.12}$$

These are irreducible tensors with respect to the orthogonal group $O(2)$. More precisely, we consider the representation of $O(2)$ on rank-2 tensors (by which a tensor T_{ab} is transformed into $g_{aa'}\,g_{bb'}\,T_{a'b'}$ for $g\in O(2)$) and decompose it in irreducible representations (IRs): two 1D IRs (scalar, corresponding to the basis tensor τ^0, and pseudoscalar, corresponding to τ^1) and a 2D IR (with basis tensors τ^2 and τ^3). (See, for example, ref. [83,p. 376] for the IR of O(2). With the notations of this reference, we have used $r^1\times r^1\simeq\varphi^1+\varphi^2+r^2$.)

We use the τ^{α}_{ab} to decompose the stress and velocity gradient tensors into irreducible components via the following definitions:

$$\oplus \triangleq \frac{1}{2}\tau^{0}_{ab}\sigma_{ab} = (\sigma_{xx}+\sigma_{yy})/2 \tag{M.13a}$$

$$\circlearrowleft \triangleq \frac{1}{2}\tau^{1}_{ab}\sigma_{ab} = (\sigma_{yx}-\sigma_{xy})/2 \tag{M.13b}$$

$$\oplus \triangleq \frac{1}{2}\tau^{2}_{ab}\sigma_{ab} = (\sigma_{xx}-\sigma_{yy})/2 \tag{M.13c}$$

$$\otimes \triangleq \frac{1}{2}\tau^{3}_{ab}\sigma_{ab} = (\sigma_{xy}+\sigma_{yx})/2 \tag{M.13d}$$

and

$$\dot{\square} \triangleq \tau^{0}_{ab}\dot{e}_{ab} = \dot{e}_{xx}+\dot{e}_{yy} \tag{M.14a}$$

$$\dot{\diamond} \triangleq \tau^{1}_{ab}\dot{e}_{ab} = \dot{e}_{yx}-\dot{e}_{xy} \tag{M.14b}$$

$$\dot{\square} \triangleq \tau^{2}_{ab}\dot{e}_{ab} = \dot{e}_{xx}-\dot{e}_{yy} \tag{M.14c}$$

$$\dot{\diamond} \triangleq \tau^{3}_{ab}\dot{e}_{ab} = \dot{e}_{xy}+\dot{e}_{yx}. \tag{M.14d}$$

Furthermore, we define the 4×4 matrix

$$\eta^{\alpha\beta} = \frac{1}{4}\tau^{\alpha}_{ab}\eta_{abcd}\tau^{\beta}_{cd} \tag{M.15}$$

in which there is a sum on repeated indices. With these definitions, equation (M.11) can be written as

$$\begin{pmatrix}\oplus\\ \circlearrowleft\\ \oplus\\ \otimes\end{pmatrix}^{\mathrm{vis}} = \begin{pmatrix}\eta^{00}&\eta^{01}&\eta^{02}&\eta^{03}\\ \eta^{10}&\eta^{11}&\eta^{12}&\eta^{13}\\ \eta^{20}&\eta^{21}&\eta^{22}&\eta^{23}\\ \eta^{30}&\eta^{31}&\eta^{32}&\eta^{33}\end{pmatrix}\begin{pmatrix}\dot{\square}\\ \dot{\diamond}\\ \dot{\square}\\ \dot{\diamond}\end{pmatrix}, \tag{M.16}$$

where the superscript 'vis' denotes the viscous stresses. Certain physical assumptions restrict the form of $\eta^{\alpha\beta}$. For example, in an isotropic system (without any other constraint), $\eta^{\alpha\beta}$ takes the form[23]

$$\eta^{\alpha\beta} = \begin{pmatrix}\zeta&\eta^{\mathrm{B}}&0&0\\ \eta^{\mathrm{A}}&\eta^{\mathrm{R}}&0&0\\ 0&0&\eta&\eta^{\mathrm{o}}\\ 0&0&-\eta^{\mathrm{o}}&\eta\end{pmatrix}. \tag{M.17}$$

The Cartesian tensors are reconstructed using

$$\sigma_{ab} = \sigma^{\alpha}\,\tau^{\alpha}_{ab} \ \text{ and } \ \dot{e}_{ab} = \frac{1}{2}\,\dot{e}^{\alpha}\,\tau^{\alpha}_{ab} \tag{M.18}$$

as well as

$$\eta_{abcd} = \eta^{\alpha\beta}\,\tau^{\alpha}_{ab}\,\tau^{\beta}_{cd}. \tag{M.19}$$

Here, we attribute no meaning to the position (subscript or superscript) of the indices (so, for instance, $\eta_{\alpha\beta}$ and $\eta^{\alpha\beta}$ mean exactly the same thing).

In standard tensor notation, equation (M.17) reads

$$\begin{aligned}\eta_{abcd} = {}& \zeta\,\delta_{ab}\delta_{cd} - \eta^{\mathrm{A}}\epsilon_{ab}\delta_{cd} - \eta^{\mathrm{B}}\delta_{ab}\epsilon_{cd} + \eta^{\mathrm{R}}\epsilon_{ab}\epsilon_{cd}\\ &+\eta\,(\delta_{ac}\delta_{bd}+\delta_{ad}\delta_{bc}-\delta_{ab}\delta_{cd}) + \eta^{\mathrm{o}}E_{abcd},\end{aligned} \tag{M.20}$$

where δ_{ab} and ϵ_{cd} denote the Kronecker delta and Levi–Civita tensors (note that $\epsilon_{ab}=\tau^{1}_{ba}$), respectively, and

$$E_{abcd} = \frac{1}{2}(\epsilon_{ac}\delta_{bd}+\epsilon_{ad}\delta_{bc}+\epsilon_{bd}\delta_{ac}+\epsilon_{bc}\delta_{ad}). \tag{M.21}$$

(Equivalently, $E_{abcd}=\epsilon_{ac}\delta_{bd}+\epsilon_{bd}\delta_{ac}$.)

When the viscosity coefficients do not depend on space, the Navier–Stokes equation

$$\rho \mathrm{D}_t\mathbf{u} = \nabla\cdot\boldsymbol{\sigma}, \ \text{ that is, } \ \rho \mathrm{D}_t u_a = \partial_b\sigma_{ab} \tag{M.22}$$

takes in isotropic chiral active fluids the general form

$$\begin{aligned}\rho \mathrm{D}_t\mathbf{u} = {}& \nabla\cdot\boldsymbol{\sigma}^{\mathrm{ss}} + \zeta\,\mathrm{grad}\,(\mathrm{div}\,\mathbf{u}) + \eta\,\Delta\mathbf{u} + \eta^{\mathrm{o}}\,\epsilon\cdot\Delta\mathbf{u}\\ &-\eta^{\mathrm{A}}\,\epsilon\cdot\mathrm{grad}\,(\mathrm{div}\,\mathbf{u}) + \eta^{\mathrm{B}}\,\mathrm{grad}\,(\mathrm{rot}\,\mathbf{u})\\ &-\eta^{\mathrm{R}}\,\epsilon\cdot\mathrm{grad}\,(\mathrm{rot}\,\mathbf{u}),\end{aligned} \tag{M.23}$$

where $\mathrm{rot}\,\mathbf{u}=\epsilon_{ab}\partial_a u_b$ and

$$\epsilon = \begin{pmatrix}0&1\\ -1&0\end{pmatrix} \tag{M.24}$$

is the matrix for rotation by $-\pi/2$.

Derivation of the fluctuating hydrodynamic theory with the Mori–Zwanzig formalism. Here, we derive the fluctuating hydrodynamic theory for chiral active fluids, by using the Mori–Zwanzig formalism[49,84–86]. This formalism provides a systematic coarse-graining procedure to decompose the microscopic dynamics of a many-body system into a hydrodynamic linear response and fluctuations induced by random stresses. Here, we give key steps of the derivation and refer the reader to Supplementary Sect. VI for more details.

We also direct the reader to refs. [87,88] and references therein for similar applications of the Mori–Zwanzig formalism in different contexts, and to refs. [89,90] for experimental investigations of the Green–Kubo relation for viscosities in dusty plasma and ref. [91] for an analysis of the density–vorticity correlations in chiral active fluids with odd viscosities.

Slow variables for momentum transfer. The dynamics of a classical many-body system can be described by its state trajectory $\boldsymbol{\Gamma}=(\mathbf{p}^{N},\mathbf{q}^{N})$ in phase space, where N is the number of particles, and $\mathbf{p}_i=m\mathbf{v}_i$ and $\mathbf{q}_i=\mathbf{r}_i$ are the momentum and position of a given particle i. For common fluids, this microscopic dynamics can be decomposed into a slow hydrodynamic behaviour plus fast fluctuations around it. The slow hydrodynamic variables are typically conserved quantities (mass, momentum, etc.) and their conservation laws, such as the Navier–Stokes equations, describe the macroscopic dynamics of the system. Fluctuating hydrodynamics accounts for the fast fluctuations through the addition of a random stress in the Navier–Stokes equation for linear momentum[39,ch. IX]. These fluctuations are ignored in usual fluid mechanics, but can become important for example at the onset of hydrodynamic instabilities and in turbulent flows. Here, we extend this treatment to the class of active fluids. Similar to conventional hydrodynamic theory, we choose momentum density as the relevant slow variable to capture momentum transfer in active fluids. In particular, we define the wavevector-dependent (reciprocal-space) momentum density of the system as

$$\hat{\mathbf{j}}_{\mathbf{k}}(t) \triangleq \sum_{i}^{N} m\mathbf{v}_i(t)\mathrm{e}^{-\mathrm{i}\mathbf{k}\cdot\mathbf{r}_i(t)}. \tag{M.25}$$

Taking the time derivative of both sides, we obtain the governing equation of $\hat{\mathbf{j}}_{\mathbf{k}}(t)$:

$$\dot{\hat{\mathbf{j}}}_{\mathbf{k}}(t) = \mathrm{i}\,\mathbf{k}\cdot\hat{\boldsymbol{\sigma}}_{\mathbf{k}}(t), \tag{M.26}$$

where $\hat{\boldsymbol{\sigma}}_{\mathbf{k}}(t)$ is the wavevector-dependent stress

$$\hat{\boldsymbol{\sigma}}_{\mathbf{k}} \triangleq -\sum_{i}^{N}\left[m\mathbf{v}_i\mathbf{v}_i + \frac{1}{2}\sum_{j\neq i}^{N-1}\mathbf{f}_{ij}\mathbf{r}_{ij}\right]\mathrm{e}^{-\mathrm{i}\mathbf{k}\cdot\mathbf{r}_i}, \tag{M.27}$$

which consistently is also the Fourier transform of the Irving–Kirkwood formula (7).

Following the same procedure, we can also define the wavevector-dependent mass density

$$\rho_{\mathbf{k}}(t) \triangleq \sum_{i}^{N} m\mathrm{e}^{-\mathrm{i}\mathbf{k}\cdot\mathbf{r}_i(t)}, \tag{M.28}$$

and derive its governing equation:

$$\dot{\rho}_{\mathbf{k}}(t) = \mathrm{i}\,\mathbf{k}\cdot\hat{\mathbf{j}}_{\mathbf{k}}(t). \tag{M.29}$$

Steady-state ensemble. The active fluids considered here reach and sustain steady state by balancing energy injection and dissipation at the microscopic level. As illustrated in Fig. 1 and Extended Figs. E1 and E2, the passive degrees of freedom are in contact with an effective bath powered by the active degrees of freedom. This gives rise to a steady-state ensemble with a stationary distribution $f_0(\boldsymbol{\Gamma})$ in the phase space.

Any observable of the system (such as the momentum density $\hat{\mathbf{j}}_{\mathbf{k}}$) corresponds to a function defined on phase space. These phase-space functions form a Hilbert space, which we denote as $\mathscr{H}(\boldsymbol{\Gamma})$. Using the probability measure $f_0(\boldsymbol{\Gamma})$, we can define the following inner product on the space $\mathscr{H}(\boldsymbol{\Gamma})$:

$$(A,B) = \langle A(\boldsymbol{\Gamma})B^{*}(\boldsymbol{\Gamma})\rangle \triangleq \int \mathrm{d}\boldsymbol{\Gamma}\,A(\boldsymbol{\Gamma})B^{*}(\boldsymbol{\Gamma})\,f_0(\boldsymbol{\Gamma}), \tag{M.30}$$

where $A(\boldsymbol{\Gamma})$ and $B(\boldsymbol{\Gamma})$ are two arbitrary phase-space functions, asterisk denotes complex conjugate and the notation $\langle\,\rangle$ defined in equation (M.30) denotes the ensemble average over $f_0(\boldsymbol{\Gamma})$. This inner product measures the similarity between two observables under the steady-state ensemble, and will allow us to separate

slow and fast variables on $\mathscr{H}(\mathbf{\Gamma})$ by defining an orthogonal projection. Given two vectors of phase-space functions $\mathbf{A}$ and $\mathbf{B}$ with components A_p and B_p, we also define the matrix $(\mathbf{A}\otimes\mathbf{B})$ with matrix elements

$$(\mathbf{A}\otimes\mathbf{B})_{pq} = (A_p, B_q). \tag{M.31}$$

This is an outer product of the vectors combined with an inner product of the phase-space functions.

Let us consider the slow variable $\hat{\mathbf{J}}_\mathbf{k}$, which is in fact a vector-valued function $\hat{\mathbf{J}}_\mathbf{k}(\mathbf{\Gamma}) = (\hat{J}_{\mathbf{k}1}(\mathbf{\Gamma}), ..., \hat{J}_{\mathbf{k}D}(\mathbf{\Gamma}))^{\mathrm{T}}$, where D is the dimension of the system. Its different components generate a subspace $\mathscr{S}_{\hat{\mathbf{J}}_\mathbf{k}}(\mathbf{\Gamma})$, and the projection operator

$$\mathcal{P}_\mathbf{k}\mathbf{X}(\mathbf{\Gamma}) \triangleq (\mathbf{X}\otimes\hat{\mathbf{J}}_\mathbf{k})\cdot(\hat{\mathbf{J}}_\mathbf{k}\otimes\hat{\mathbf{J}}_\mathbf{k})^{-1}\cdot\hat{\mathbf{J}}_\mathbf{k} \tag{M.32}$$

performs an orthogonal projection on this subspace. We also define the projection operator to the orthogonal subspace:

$$\mathcal{Q}_\mathbf{k} = 1 - \mathcal{P}_\mathbf{k}. \tag{M.33}$$

In equation (M.32), the normalization matrix $(\hat{\mathbf{J}}_\mathbf{k}\otimes\hat{\mathbf{J}}_\mathbf{k})$ quantifies the correlations between different components of the momentum density at steady state, with the form

$$(\hat{\mathbf{J}}_\mathbf{k}\otimes\hat{\mathbf{J}}_\mathbf{k}) = m^2N\left[\frac{k_\mathrm{B}T_\mathrm{eff}}{m}\mathcal{I} + n\hat{\mathcal{C}}_{\mathbf{vv}}(\mathbf{k})\right], \tag{M.34}$$

where $\mathcal{I}$ is a $D\times D$ identity matrix, n is the number density of the particles and $\hat{\mathcal{C}}_{\mathbf{vv}}(\mathbf{k})$ is the Fourier transform of the velocity–velocity correlation matrix

$$\hat{\mathcal{C}}_{\mathbf{vv}}(\mathbf{r}) = \langle\mathbf{v}(\mathbf{r})\,\mathbf{v}(0)\rangle. \tag{M.35}$$

In common fluids, interactions between fluid particles are conservative and only depend on interparticle distance. This allows the factorization of the Boltzmann distribution into momentum and position parts:

$$P(\mathbf{\Gamma}) \propto \mathrm{e}^{-\sum_i mv_i^2/2k_\mathrm{B}T}\times\mathrm{e}^{-\sum_{ij}U(\mathbf{r}_{ij})/k_\mathrm{B}T}. \tag{M.36}$$

Hence, the velocities of different particles are independent, and $\hat{\mathcal{C}}_{\mathbf{vv}}(\mathbf{k})$ vanishes.

However, this is not generally the case for non-equilibrium fluids related to velocity-dependent interactions, including our chiral active fluid. By assuming the isotropy of the system and a fast decaying correlation function $|\hat{\mathcal{C}}_{\mathbf{vv}}(\mathbf{r})| < \mathcal{O}(r^{-D})$, we show that

$$(\hat{\mathbf{J}}_\mathbf{k}\otimes\hat{\mathbf{J}}_\mathbf{k}) \approx Nm\,(k_\mathrm{B}T_\mathrm{eff} + B_{\mathbf{vv}})\,\mathcal{I}, \tag{M.37}$$

in which

$$B_{\mathbf{vv}} \triangleq \frac{nm}{D}\lim_{\mathbf{k}\to0}\int_V\langle\mathbf{v}(\mathbf{r})\cdot\mathbf{v}(0)\rangle\,\mathrm{e}^{-\mathrm{i}\mathbf{k}\cdot\mathbf{r}}\,\mathrm{d}\,\mathbf{r}. \tag{M.38}$$

For convenience, we define

$$T^*_\mathrm{eff} = T_\mathrm{eff} + B_{\mathbf{vv}}/k_\mathrm{B}. \tag{M.39}$$

Mori–Zwanzig formalism. Now we can use the projection operators $\mathcal{P}_\mathbf{k}$ and $\mathcal{Q}_\mathbf{k}$ to decompose the evolution of the momentum density $\hat{\mathbf{J}}_\mathbf{k}$ into a slow dynamics within the subspace $\mathscr{S}_{\hat{\mathbf{J}}_\mathbf{k}}(\mathbf{\Gamma})$ and fast fluctuations orthogonal to it. This is the main idea of the Mori–Zwanzig formalism.

One can show that the governing equation (M.26) is also a Liouvillian equation:

$$\dot{\hat{\mathbf{J}}}_\mathbf{k}(t) = \mathrm{i}\,\mathcal{L}\hat{\mathbf{J}}_\mathbf{k}(t), \tag{M.40}$$

where

$$\mathrm{i}\,\mathcal{L} \triangleq \dot{\mathbf{\Gamma}}\cdot\frac{\partial}{\partial\mathbf{\Gamma}} \tag{M.41}$$

denotes the Liouville operator. Using the Mori–Zwanzig formalism, we decompose the above equation as

$$\dot{\hat{\mathbf{J}}}_\mathbf{k}(t) = \mathbf{F}^{\parallel}_\mathbf{k}(t) + \mathbf{F}^{\perp}_\mathbf{k}(t) - \int_0^t\mathbf{K}(\tau)\cdot\hat{\mathbf{J}}_\mathbf{k}(t-\tau)\,\mathrm{d}\,\tau, \tag{M.42}$$

where

$$\mathbf{F}^{\parallel}_\mathbf{k}(t) \triangleq \mathrm{e}^{\mathrm{i}\mathcal{L}t}\mathcal{P}_\mathbf{k}\,\mathrm{i}\,\mathcal{L}\hat{\mathbf{J}}_\mathbf{k}(\mathbf{\Gamma}), \tag{M.43}$$

$$\mathbf{F}^{\perp}_\mathbf{k}(t) \triangleq \mathrm{e}^{\mathcal{Q}_\mathbf{k}\mathrm{i}\mathcal{L}t}\mathcal{Q}_\mathbf{k}\,\mathrm{i}\,\mathcal{L}\hat{\mathbf{J}}_\mathbf{k}(\mathbf{\Gamma}), \tag{M.44}$$

$$\mathbf{K}(\tau) \triangleq (\mathbf{F}^{\perp}_\mathbf{k}(\tau)\otimes\mathbf{F}^{\perp}_\mathbf{k}(0))\cdot(\hat{\mathbf{J}}_\mathbf{k}\otimes\hat{\mathbf{J}}_\mathbf{k})^{-1}. \tag{M.45}$$

Here, $\mathbf{F}^{\parallel}_\mathbf{k}(\mathbf{\Gamma}, t)$ and $\mathbf{F}^{\perp}_\mathbf{k}(\mathbf{\Gamma}, t)$ are the components of the generalized force $\mathrm{i}\,\mathcal{L}\hat{\mathbf{J}}_\mathbf{k}(t)$ parallel and orthogonal to the subspace $\mathscr{S}_{\hat{\mathbf{J}}_\mathbf{k}}(\mathbf{\Gamma})$, and $\mathbf{K}(\tau)$ is a kernel function characterizing the linear response of the fluid towards external disturbances on $\hat{\mathbf{J}}_\mathbf{k}$. Note that $\mathbf{K}(\tau)$ involves the calculation of time correlation functions, which requires performing ensemble averages at different time points. For systems with deterministic microscopic dynamics, we can generalize equation (M.30) to calculate the time correlation function with equal-time probability $f_0(\mathbf{\Gamma})$:

$$\begin{aligned}(A(t), B(0)) &= \langle A(\mathbf{\Gamma}_t)B^*(\mathbf{\Gamma}_0)\rangle\\ &= \int\mathrm{d}\,\mathbf{\Gamma}\;\mathcal{Q}_A(\mathbf{\Gamma}, t)A(\mathbf{\Gamma})\cdot B(\mathbf{\Gamma})\cdot f_0(\mathbf{\Gamma}),\end{aligned} \tag{M.46}$$

where $\mathcal{Q}_A(\mathbf{\Gamma}, t)$ is the propagator of the phase-space function A and we have used $\mathbf{\Gamma}=\mathbf{\Gamma}_0$ to represent the phase space at the initial state $t=0$. In the case of equation (M.45), $A = B = \mathbf{F}^{\perp}_\mathbf{k}$, $\mathcal{Q}_A(\mathbf{\Gamma}, t) = \mathrm{e}^{\mathcal{Q}_\mathbf{k}\mathrm{i}\mathcal{L}t}$.

Extra care must be taken when applying the formalism to active fluids. A crucial step in the derivation of equation (M.42) is

$$(\,\mathrm{i}\,\mathcal{L}\mathbf{F}^{\perp}_\mathbf{k}(\tau)\otimes\hat{\mathbf{J}}_\mathbf{k}) = -(\mathbf{F}^{\perp}_\mathbf{k}(\tau)\otimes\,\mathrm{i}\,\mathcal{L}\hat{\mathbf{J}}_\mathbf{k}). \tag{M.47}$$

A key insight is that this relation still holds near any non-equilibrium steady state, even when detailed balance is broken. At steady state, the probability distribution does not change over time, thus

$$\frac{\mathrm{d}}{\mathrm{d}\,t}f_0(\mathbf{\Gamma}) = \frac{\partial}{\partial\mathbf{\Gamma}}(\dot{\mathbf{\Gamma}}f_0(\mathbf{\Gamma})) = 0. \tag{M.48}$$

Given the assumption of the existence of a steady state, one can prove equation (M.47) elementwise using integration by parts:

$$\begin{aligned}&(\mathrm{i}\mathcal{L}\mathbf{F}^{\perp}_\mathbf{k}(\tau)\otimes\hat{\mathbf{J}}_\mathbf{k})_{ab} + (\mathbf{F}^{\perp}_\mathbf{k}(\tau)\otimes\mathrm{i}\mathcal{L}\hat{\mathbf{J}}_\mathbf{k})_{ab}\\ &= -\int\mathrm{d}\,\mathbf{\Gamma}F^{\perp}_{\mathbf{k},a}(\mathbf{\Gamma}, \tau)\hat{J}^*_{\mathbf{k},b}(\mathbf{\Gamma})\cdot\tfrac{\partial}{\partial\mathbf{\Gamma}}(\dot{\mathbf{\Gamma}}f_0(\mathbf{\Gamma})) = 0.\end{aligned} \tag{M.49}$$

In this case, the Liouvillian is Hermitian with respect to the inner product defined by f_0 and the decomposition given by equation (M.42) still holds.

Generalized forces. To make use of the Mori–Zwanzig formalism, we must derive the explicit form of $\mathbf{F}^{\parallel}_\mathbf{k}$, $\mathbf{F}^{\perp}_\mathbf{k}$ and $\mathbf{K}$.

For active fluids, the generalized force contains three components:

$$\mathrm{i}\,\mathcal{L}\hat{\mathbf{J}}_\mathbf{k} = \mathrm{i}\,\mathbf{k}\cdot\hat{\boldsymbol{\sigma}}_\mathbf{k} = \mathrm{i}\,\mathbf{k}\cdot\left(\hat{\boldsymbol{\sigma}}^{\mathrm{kin}}_\mathbf{k} + \hat{\boldsymbol{\sigma}}^{\mathrm{pos}}_\mathbf{k} + \hat{\boldsymbol{\sigma}}^{\mathrm{vel}}_\mathbf{k}\right), \tag{M.50}$$

with

$$\hat{\boldsymbol{\sigma}}^{\mathrm{kin}}_\mathbf{k} \triangleq -\sum_i^N m\mathbf{v}_i\mathbf{v}_i\,\mathrm{e}^{-\mathrm{i}\mathbf{k}\cdot\mathbf{r}_i} \tag{M.51}$$

$$\hat{\boldsymbol{\sigma}}^{\mathrm{pos}}_\mathbf{k} \triangleq -\frac{1}{2}\sum_{ij}^{N^2}\mathbf{f}^{\mathrm{pos}}_{ij}\,\mathbf{r}_{ij}\mathrm{e}^{-\mathrm{i}\mathbf{k}\cdot\mathbf{r}_i}, \tag{M.52}$$

$$\hat{\boldsymbol{\sigma}}^{\mathrm{vel}}_\mathbf{k} \triangleq -\frac{1}{2}\sum_{ij}^{N^2}\mathbf{f}^{\mathrm{vel}}_{ij}\,\mathbf{r}_{ij}\mathrm{e}^{-\mathrm{i}\mathbf{k}\cdot\mathbf{r}_i}, \tag{M.53}$$

where $\hat{\boldsymbol{\sigma}}^{\mathrm{kin}}_\mathbf{k}$ is the kinetic stress, $\hat{\boldsymbol{\sigma}}^{\mathrm{pos}}_\mathbf{k}$ is the virial stress only involving the position-dependent interactions $\mathbf{f}^{\mathrm{pos}}_{ij}$ and $\hat{\boldsymbol{\sigma}}^{\mathrm{vel}}_\mathbf{k}$ is the virial stress caused by velocity-dependent interactions, which is unique to non-equilibrium fluids. Here we assume that the velocity-dependent interactions come from interparticle friction, taking a general form $\mathbf{f}^{\mathrm{vel}}_{ij} = -\gamma(r_{ij})\,\mathbf{v}_{ij}$.

The presence of the interparticle friction as well as the resultant velocity–velocity correlations poses a major challenge in our derivation, making it different from the textbook derivation of the Green–Kubo relation for viscosity using the Mori–Zwanzig formalism[86]. By assuming that the three-body (and higher-order) correlations are negligible, we can derive the explicit form of the generalized forces:

$$\mathbf{F}^{\parallel}_\mathbf{k}(t) = -\gamma_{\hat{\mathbf{J}}_\mathbf{k}}\hat{\mathbf{J}}_\mathbf{k}(t), \tag{M.54}$$

$$\mathbf{F}^{\perp}_\mathbf{k}(t) \approx \gamma_{\hat{\mathbf{J}}_\mathbf{k}}\hat{\mathbf{J}}_\mathbf{k}(t) + \mathrm{i}\,\mathbf{k}\cdot\hat{\boldsymbol{\sigma}}_\mathbf{k}(t), \tag{M.55}$$

where $\gamma_{\hat{\mathbf{J}}_\mathbf{k}} = n(\hat{\gamma}(0) - \hat{\gamma}(k))/m$ denotes the wavevector-dependent effective damping parameter for $\hat{\mathbf{J}}_\mathbf{k}$. Here, $\hat{\gamma}(k) = \int_V\gamma(r)\mathrm{e}^{-\mathrm{i}\mathbf{k}\cdot\mathbf{r}}\,\mathrm{d}\,\mathbf{r}$ denotes the Fourier transform of the interparticle frictional kernel $\gamma(r)$. With that, we can also derive the form of the response kernel:

$$\mathbf{K}(\tau) = -\gamma_{\hat{\mathbf{J}}_\mathbf{k}}^2 \left(\hat{\mathbf{J}}_\mathbf{k}(\tau) \otimes \hat{\mathbf{J}}_\mathbf{k}(0)\right) \cdot (\hat{\mathbf{J}}_\mathbf{k} \otimes \hat{\mathbf{J}}_\mathbf{k})^{-1} + (\mathrm{i}\,\mathbf{k} \cdot \hat{\boldsymbol{\sigma}}_\mathbf{k}(\tau) \otimes \mathrm{i}\,\mathbf{k} \cdot \hat{\boldsymbol{\sigma}}_\mathbf{k}(0)) \cdot (\hat{\mathbf{J}}_\mathbf{k} \otimes \hat{\mathbf{J}}_\mathbf{k})^{-1}. \tag{M.56}$$

Detailed derivation steps are provided in Supplementary Sect. VI.

Green–Kubo relation. For a system in non-equilibrium steady state, the noise term $\mathbf{F}_\mathbf{k}^\perp$ vanishes in equation (M.42) under an ensemble average. Thus, in an average sense, the governing equation (M.26) reads

$$\dot{\hat{\mathbf{J}}}_\mathbf{k}(t) = \mathbf{F}_\mathbf{k}^\parallel(t) - \int_0^t \mathrm{d}\tau\, \mathbf{K}(\tau) \cdot \hat{\mathbf{J}}_\mathbf{k}(t-\tau). \tag{M.57}$$

By plugging the explicit form of $\mathbf{F}_\mathbf{k}^\parallel$ and $\mathbf{K}$ and taking Laplace transform, we can obtain the following equation:

$$s\widetilde{\mathbf{J}}_\mathbf{k}(s) - \hat{\mathbf{J}}_\mathbf{k}(0) = -\frac{\left(\mathrm{i}\,\mathbf{k} \cdot \widetilde{\boldsymbol{\sigma}}_\mathbf{k}(s) \otimes \mathrm{i}\,\mathbf{k} \cdot \hat{\boldsymbol{\sigma}}_\mathbf{k}(0)\right) \cdot \widetilde{\mathbf{J}}_\mathbf{k}(s)}{Nmk_\mathrm{B}T_\mathrm{eff}^*}. \tag{M.58}$$

Note that the right-hand side of the above equation is a linear response in momentum density $\hat{\mathbf{J}}_\mathbf{k}$. Given the wavevector-dependent strain rate $\hat{\dot{e}}_{\mathbf{k},cd} = \mathrm{i}\,k_d\hat{J}_{\mathbf{k},c}/nm$, we find that equation (M.58) in fact corresponds to a hydrodynamic linear response

$$s\widetilde{J}_{\mathbf{k},a}(s) - \hat{J}_{\mathbf{k},a}(0) = \mathrm{i}\,k_b\,\widetilde{\eta}_{\mathbf{k},abcd}(s)\,\widetilde{\dot{e}}_{\mathbf{k},cd}(s) \tag{M.59}$$

with viscosity coefficients

$$\widetilde{\eta}_{\mathbf{k},abcd}(s) \triangleq \frac{1}{k_\mathrm{B}T_\mathrm{eff}^* V}\langle\widetilde{\sigma}_{\mathbf{k},ab}(s)\hat{\sigma}_{\mathbf{k},cd}^*(0)\rangle. \tag{M.60}$$

Here, we switched to index notation and used the Einstein summation rule for the indices. In the hydrodynamic limit, equation (M.60) becomes the equilibrium-like Green–Kubo relation for the viscosity

$$\eta_{abcd} = \lim_{\substack{\mathbf{k}\to 0\\ s\to 0}} \widetilde{\eta}_{\mathbf{k},abcd}(s) = \frac{V}{k_\mathrm{B}T_\mathrm{eff}^*}\int_0^\infty \langle\sigma_{ab}(t)\sigma_{cd}(0)\rangle\,\mathrm{d}t, \tag{M.61}$$

which is equivalent to equation (11) in terms of the irreducible representations of stress. Note that, in the above formula, we have used the global stress $\boldsymbol{\sigma}(t) = \int_V \boldsymbol{\sigma}(\mathbf{r}, t)\,\mathrm{d}\mathbf{r}/V$.

Hydrodynamic equations. Our previous derivation was performed near steady state with a vanishing background flow field $\mathbf{u}(\mathbf{r}) = 0$ everywhere. Here we extend our theory to the hydrodynamic behaviour with non-zero background flow field. Let us first define the density, momentum and stress fields:

$$\rho(\mathbf{r}) = \sum_i^N m\,\delta(\mathbf{r} - \mathbf{r}_i), \tag{M.62}$$

$$\mathbf{J}(\mathbf{r}) = \sum_i^N m\mathbf{v}_i\,\delta(\mathbf{r} - \mathbf{r}_i), \tag{M.63}$$

$$\boldsymbol{\sigma}(\mathbf{r}) = -\sum_i^N \left[m\mathbf{v}_i\mathbf{v}_i + \frac{1}{2}\sum_{j\neq i}^{N-1}\mathbf{f}_{ij}\mathbf{r}_{ij}\right]\delta(\mathbf{r} - \mathbf{r}_i). \tag{M.64}$$

Note that these are also the inverse Fourier transforms of $\rho_\mathbf{k}$, $\hat{\mathbf{J}}_\mathbf{k}$ and $\hat{\boldsymbol{\sigma}}_\mathbf{k}$ defined above. In addition, the flow field is defined as

$$\mathbf{u}(\mathbf{r}) = \frac{\mathbf{J}(\mathbf{r})}{\rho(\mathbf{r})}. \tag{M.65}$$

In a common fluid, the fluid elements stay near local thermal equilibrium. Similarly, we assume that the particles in an active fluid stay close to local steady state. Under these assumptions, we can decompose the particle velocity as

$$\mathbf{v} = \mathbf{u}(\mathbf{r}, t) + \Delta\mathbf{v}, \tag{M.66}$$

where $\mathbf{u}(\mathbf{r}, t)$ is the local flow field and $\Delta\mathbf{v}$ is the velocity fluctuation on top of it. These two terms satisfy

$$\langle\Delta\mathbf{v}\rangle = 0, \quad \langle\mathbf{u}(\mathbf{r}, t)\,\Delta\mathbf{v}\rangle = 0. \tag{M.67}$$

The interaction of a particle with its neighbours depends on their relative rather than average velocity. Thus, we assume that, by subtracting the local flow field $\mathbf{u}(\mathbf{r})$, the local ensemble is the same as the global one at steady state. This allows us to decompose the stress field $\boldsymbol{\sigma}(\mathbf{r})$ as

$$\boldsymbol{\sigma} = -\rho\mathbf{u}\mathbf{u} + \boldsymbol{\sigma}^\mathrm{IK}, \tag{M.68}$$

where $\rho\mathbf{u}\mathbf{u}$ is the dynamical pressure due to fluid flow and $\boldsymbol{\sigma}^\mathrm{IK}$ is the Irving–Kirkwood stress,

$$\boldsymbol{\sigma}^\mathrm{IK}(\mathbf{r}) \triangleq -\sum_i^N \left[m\Delta\mathbf{v}_i\Delta\mathbf{v}_i + \frac{1}{2}\sum_{j\neq i}^{N-1}\mathbf{f}_{ij}\mathbf{r}_{ij}\right]\delta(\mathbf{r} - \mathbf{r}_i). \tag{M.69}$$

The Irving–Kirkwood stress can be further decomposed into three parts: (i) the isotropic steady-state stress given by the equations of state

$$\sigma_{ab}^\mathrm{ss} = \begin{cases} -P\,\delta_{ab} + \tau\,\epsilon_{ab}, & \text{in 2D} \\ -P\,\delta_{ab}, & \text{in 3D} \end{cases} \tag{M.70}$$

(in 3D, the presence of an anti-symmetric steady-state stress is prohibited by isotropy), (ii) the viscous stress due to hydrodynamic linear response

$$\sigma_{ab}^\mathrm{vis} = \eta_{abcd}\,\dot{e}_{cd}, \tag{M.71}$$

and (iii) the random stress arising from the orthogonal generalized force satisfying the relation

$$\mathrm{i}\,k_b\,\hat{\sigma}_{\mathbf{k},ab}^\mathrm{R} = \hat{F}_{\mathbf{k},a}^\perp. \tag{M.72}$$

With that, we can then get the hydrodynamic equations by performing the inverse Fourier transform of equations (M.26) and (M.29), giving

$$D_t\rho = -\rho\nabla\cdot\mathbf{u}, \tag{M.73a}$$

$$\rho D_t\mathbf{u} = \nabla\cdot\left(\boldsymbol{\sigma}^\mathrm{ss} + \boldsymbol{\sigma}^\mathrm{vis} + \boldsymbol{\sigma}^\mathrm{R}\right), \tag{M.73b}$$

where $D_t = \partial_t + \mathbf{u}\cdot\nabla$ is the material derivative.

Random stress. To complete our fluctuating hydrodynamic theory, we need to derive the form of the random stress $\boldsymbol{\sigma}^\mathrm{R}$. Recall that the explicit form of the orthogonal generalized force is

$$\mathbf{F}_\mathbf{k}^\perp(t) \approx \gamma_{\hat{\mathbf{J}}_\mathbf{k}}\hat{\mathbf{J}}_\mathbf{k}(t) + \mathrm{i}\,\mathbf{k}\cdot\hat{\boldsymbol{\sigma}}_\mathbf{k}(t). \tag{M.74}$$

Using the homogeneity of the system at steady state, we show that $\mathbf{F}_\mathbf{k}^\perp$ is indeed a random force with zero mean

$$\langle\mathbf{F}_\mathbf{k}^\perp\rangle = 0. \tag{M.75}$$

We also find that

$$\gamma_{\hat{\mathbf{J}}_\mathbf{k}} = \frac{n}{m}\int_V \gamma(r)(1 - \mathrm{e}^{-\mathrm{i}\mathbf{k}\cdot\mathbf{r}})\,\mathrm{d}\mathbf{r} = \left[\tfrac{2\pi n}{3m}\int_0^\infty \gamma(r)r^4\,dr\right]k^2 + \mathcal{O}(k^3). \tag{M.76}$$

Therefore, we can drop the first term in the calculation of the two-point correlations and get

$$\langle F_{\mathbf{k},a}^\perp(t)\,F_{\mathbf{k},c}^{\perp *}(0)\rangle \approx k_b\langle\hat{\sigma}_{\mathbf{k},ab}(t)\,\hat{\sigma}_{\mathbf{k},cd}^*(0)\rangle k_d. \tag{M.77}$$

Given relation (M.60), one can further show that

$$\langle\widetilde{F}_{\mathbf{k},a}^\perp(s)\,F_{\mathbf{k},c}^{\perp *}(0)\rangle = k_\mathrm{B}T_\mathrm{eff}^* V\,\widetilde{\eta}_{\mathbf{k},abcd}(s)\,k_b k_d. \tag{M.78}$$

Note that s is the parameter for Laplace transforms. Hence, we should construct the random stress $\boldsymbol{\sigma}^\mathrm{R}$ as

$$\langle\hat{\sigma}_{\mathbf{k},ab}^\mathrm{R}\rangle = 0, \tag{M.79}$$

$$\langle\hat{\sigma}_{\mathbf{k},ab}^\mathrm{R}(s)\,\hat{\sigma}_{\mathbf{k},cd}^{\mathrm{R}\,*}(0)\rangle = k_\mathrm{B}T_\mathrm{eff}^*\,\widetilde{\eta}_{\mathbf{k},abcd}(s). \tag{M.80}$$

In the hydrodynamic limit, the correlation time and length of the random stress become negligible compared with that of the hydrodynamic flow. In this case, the above requirements can also be written as

$$\begin{aligned}\langle\sigma_{ab}^\mathrm{R}(\mathbf{r}, t)\rangle &= 0 \\ \langle\sigma_{ab}^\mathrm{R}(\mathbf{r}, t)\sigma_{cd}^\mathrm{R}(0, 0)\rangle &= 2k_\mathrm{B}T_\mathrm{eff}^*\,\delta(\mathbf{r})\left[\eta_{abcd}^\mathrm{sym}\delta(t) + \eta_{abcd}^\mathrm{anti}\,\xi(t)\right],\end{aligned} \tag{M.81}$$

where $\eta_{abcd}^\mathrm{sym} = (\eta_{abcd} + \eta_{cdab})/2$ and $\eta_{abcd}^\mathrm{anti} = (\eta_{abcd} - \eta_{cdab})/2$ are the symmetric and anti-symmetric parts of the viscosity tensor under the exchange of major indices, that is, $ab \leftrightarrow cd$. In practice, the Dirac distribution in equation (M.81) has a finite width τ and can be represented, for instance, by a Gaussian function

$$\delta_\tau(t) \triangleq \frac{1}{\sqrt{2\pi}\,\tau} \mathrm{e}^{-\frac{t^2}{2\tau^2}}. \tag{M.82}$$

Similarly, $\xi(t)$ stands in equation (M.81) for a function $\xi_\tau(t)$ defined as

$$\xi_\tau(t) \triangleq \frac{t}{2\tau^2} \mathrm{e}^{-\frac{t^2}{2\tau^2}}. \tag{M.83}$$

This is an odd function, satisfying the relations

$$\xi(t) = -\xi(-t), 2\int_0^\infty \xi(t)\ \mathrm{d}t = 1.$$

Upon decomposition of the stresses into their irreducible representations, equation (M.81) becomes equation (9) in the main text. By integrating equation (M.81) in both space and time, we get the Green–Kubo relation:

$$\int_0^\infty \mathrm{d}t \int_V \mathrm{d}\mathbf{r}\ \left\langle \sigma^{\mathrm{R}}_{ab}(\mathbf{r},t)\sigma^{\mathrm{R}}_{cd}(0,0)\right\rangle = k_{\mathrm{B}}T^*_{\mathrm{eff}}\eta_{abcd}. \tag{M.84}$$

We emphasize that the term $\eta^{\mathrm{anti}}_{abcd}\xi(t)$ changes sign when $t\to -t$. This is crucial to obtain the anti-symmetric part of the viscosity tensor in the Green–Kubo relation, and consistent with intuitions from the usual Onsager–Casimir relations. For common fluids, the random stress is often chosen as a white noise in the conventional fluctuating hydrodynamic theory. However, for non-equilibrium fluids, especially chiral active fluids, extra care must be taken: the construction of the random stress should reflect the time-reversal symmetry/anti-symmetry of the system.

Data availability

The data that supports all the plots in this paper are available at https://doi.org/10.5281/zenodo.5138328. Source data are provided with this paper.

Code availability

The simulation codes used in this study are available upon request.

References

53. Drescher, K. et al. Dancing volvox: hydrodynamic bound states of swimming algae. *Phys. Rev. Lett.* **102**, 168101 (2009).
54. Kokot, G. & Snezhko, A. Manipulation of emergent vortices in swarms of magnetic rollers. *Nat. Commun.* **9**, 2344 (2018).
55. Lei, Q.-L., Ciamarra, M. P. & Ni, R. Nonequilibrium strongly hyperuniform fluids of circle active particles with large local density fluctuations. *Sci. Adv.* **5**, eaau7423 (2019).
56. Lei, Q.-L. & Ni, R. Hydrodynamics of random-organizing hyperuniform fluids. *Proc. Natl Acad. Sci. USA* **116**, 22983–22989 (2019).
57. Plimpton, S., Kohlmeyer, A., Thompson, A., Moore, S. & Berger, R. Lammps stable release 29 october 2020 (2020).
58. Plimpton, S. Fast parallel algorithms for short-range molecular dynamics. *J. Comput. Phys.* **117**, 1–19 (1995).
59. Han, M., Yan, J., Granick, S. & Luijten, E. Effective temperature concept evaluated in an active colloid mixture. *Proc. Natl Acad. Sci. USA* **114**, 7513–7518 (2017).
60. Yan, J., Bae, S. C. & Granick, S. Rotating crystals of magnetic janus colloids. *Soft Matter* **11**, 147–153 (2015).
61. Reeves, C. J., Aranson, I. S. & Vlahovska, P. M. Emergence of lanes and turbulent-like motion in active spinner fluid. *Commun. Phys.* https://doi.org/10.1038/s42005-021-00596-2 (2021).
62. LeGoff, L., Amblard, F. & Furst, E. M. Motor-driven dynamics in actin–myosin networks. *Phys. Rev. Lett.* **88**, 018101 (2001).
63. Berthier, L. & Kurchan, J. Non-equilibrium glass transitions in driven and active matter. *Nat. Phys.* **9**, 310 (2013).
64. Palacci, J., Cottin-Bizonne, C., Ybert, C. & Bocquet, L. Sedimentation and effective temperature of active colloidal suspensions. *Phys. Rev. Lett.* **105**, 088304 (2010).
65. Chvykov, P. et al. Low rattling: a predictive principle for self-organization in active collectives. *Science* **371**, 90–95 (2021).
66. Egolf, D. A. Equilibrium regained: from nonequilibrium chaos to statistical mechanics. *Science* **287**, 101–104 (2000).
67. Dahler, J. S. & Scriven, L. E. Angular momentum of continua. *Nature* **192**, 36–37 (1961).
68. Snider, R. F. & Lewchuk, K. S. Irreversible thermodynamics of a fluid system with spin. *J. Chem. Phys.* **46**, 3163–3172 (1967).
69. Evans, D. J. On the generalized hydrodynamics of polyatomic fluids. *Mol. Phys.* **32**, 1171–1176 (1976).
70. Schofield, P. & Henderson, J. R. Statistical mechanics of inhomogeneous fluids. *Proc. R. Soc. A* **379**, 231–246 (1982).
71. Goldhirsch, I. Stress, stress asymmetry and couple stress: from discrete particles to continuous fields. *Granul. Matter* **12**, 239–252 (2010).
72. Harada, T. & Sasa, S.-i Equality connecting energy dissipation with a violation of the fluctuation–response relation. *Phys. Rev. Lett.* **95**, 130602 (2005).
73. Fodor, É. et al. How far from equilibrium is active matter? *Phys. Rev. Lett.* **117**, 038103 (2016).
74. Prost, J., Joanny, J.-F. & Parrondo, J. Generalized fluctuation–dissipation theorem for steady-state systems. *Phys. Rev. Lett.* **103**, 090601 (2009).
75. Gomez-Solano, J. R., Petrosyan, A., Ciliberto, S., Chetrite, R. & Gawędzki, K. Experimental verification of a modified fluctuation-dissipation relation for a micron-sized particle in a nonequilibrium steady state. *Phys. Rev. Lett.* **103**, 040601 (2009).
76. Seifert, U. & Speck, T. Fluctuation–dissipation theorem in nonequilibrium steady states. *Europhys. Lett.* **89**, 10007 (2010).
77. Cengio S. D., Levis D., and Pagonabarraga I. Linear response theory and Green–Kubo relations for active matter. Preprint at http://arxiv.org/abs/1907.02560 (2019).
78. Sarracino, A. & Vulpiani, A. On the fluctuation–dissipation relation in non-equilibrium and non-hamiltonian systems. *Chaos* **29**, 083132 (2019).
79. Shankar, S. & Marchetti, M. C. Hidden entropy production and work fluctuations in an ideal active gas. *Phys. Rev. E* **98**, 020604 (2018).
80. Puglisi, A., Baldassarri, A. & Vulpiani, A. Violation of the Einstein relation in granular fluids: the role of correlations. *J. Stat. Mech. Theory Exp.* **2007**, P08016–P08016 (2007).
81. Visco, P. Work fluctuations for a Brownian particle between two thermostats. *J. Stat. Mech.: Theory Exp.* **2006**, P06006–P06006 (2006).
82. Horowitz, J. M. & Gingrich, T. R. Thermodynamic uncertainty relations constrain non-equilibrium fluctuations. *Nat. Phys.* **16**, 15–20 (2019).
83. Sternberg, S. *Group Theory and Physics* (Cambridge Univ. Press, 1995).
84. Mori, H. Transport, collective motion, and brownian motion. *Prog. Theor. Exp. Phys.* **33**, 423–455 (1965).
85. Nakajima, S. On quantum theory of transport phenomena. *Prog. Theor. Exp. Phys.* **20**, 948–959 (1958).
86. Zwanzig, R. Ensemble method in the theory of irreversibility. *J. Chem. Phys.* **33**, 1338–1341 (1960).
87. Ihle, T. & Kroll, D. M. Stochastic rotation dynamics. I. formalism, Galilean invariance, and Green–Kubo relations. *Phys. Rev. E* **67**, 066705 (2003).
88. Krommes, J. A. Projection-operator methods for classical transport in magnetized plasmas. Part 1. Linear response, the Braginskii equations and fluctuating hydrodynamics. *J. Plasma Phys.* **84**, 925840401 (2018).
89. Feng, Y., Goree, J., Liu, B. & Cohen, E. G. D. Green–Kubo relation for viscosity tested using experimental data for a two-dimensional dusty plasma. *Phys. Rev. E* **84**, 046412 (2011).
90. Haralson, Z. & Goree, J. Overestimation of viscosity by the Green–Kubo method in a dusty plasma experiment. *Phys. Rev. Lett.* **118**, 195001 (2017).
91. Banerjee, D., Souslov, A. & Vitelli, V. Hydrodynamic correlation functions of chiral active fluids. Preprint at http://arxiv.org/abs/2005.00621 (2020).

Acknowledgements

The authors thank A. G. Abanov, S. Atis, D. Bartolo, W. T. M. Irvine, C. Nardini, H. C. Öttinger and D. T. Son for helpful discussions and suggestions. S.V., J.J.d.P. and V.V. acknowledge primary support through the Chicago MRSEC, funded by the NSF through grant no. DMR-1420709. S.V. acknowledges support from the National Science Foundation under grant no. DMR-1848306. V.V. acknowledges support from the Complex Dynamics and Systems Program of the Army Research Office under grant no. W911NF-19-1-0268, the Simons Foundation and the KITP program on Symmetry, Thermodynamics and Topology in Active Matter via NSF grant no. PHY-1748958. M.H. and M.F. acknowledge support from the University of Chicago MRSEC through Kadanoff–Rice postdoctoral fellowships. C.S. acknowledges support by the National Science Foundation Graduate Research Fellowship under grant no. 1746045. M.H. acknowledges use of the GM4 cluster supported by the National Science Foundation's Division of Materials Research under the Major Research Instrumentation (MRI) program award no. 1828629. This work was completed in part with resources provided by the University of Chicago's Research Computing Center. Calculations presented here were performed on the GPU cluster supported by the NSF under grant DMR-1828629.

Author contributions

M.H. performed the simulations and analysed the data. All authors conducted theoretical research. M.H., M.F., C.S. and V.V. wrote the paper. All authors contributed to discussions, interpretation of the results and manuscript revision.

Competing interests

The authors declare no competing financial interests.

Additional information

Extended data is available for this paper at https://doi.org/10.1038/s41567-021-01360-7.

Supplementary information The online version contains supplementary material available at https://doi.org/10.1038/s41567-021-01360-7.

Correspondence and requests for materials should be addressed to Vincenzo Vitelli.

Peer review information *Nature Physics* thanks the anonymous reviewers for their contribution to the peer review of this work.

Reprints and permissions information is available at www.nature.com/reprints.

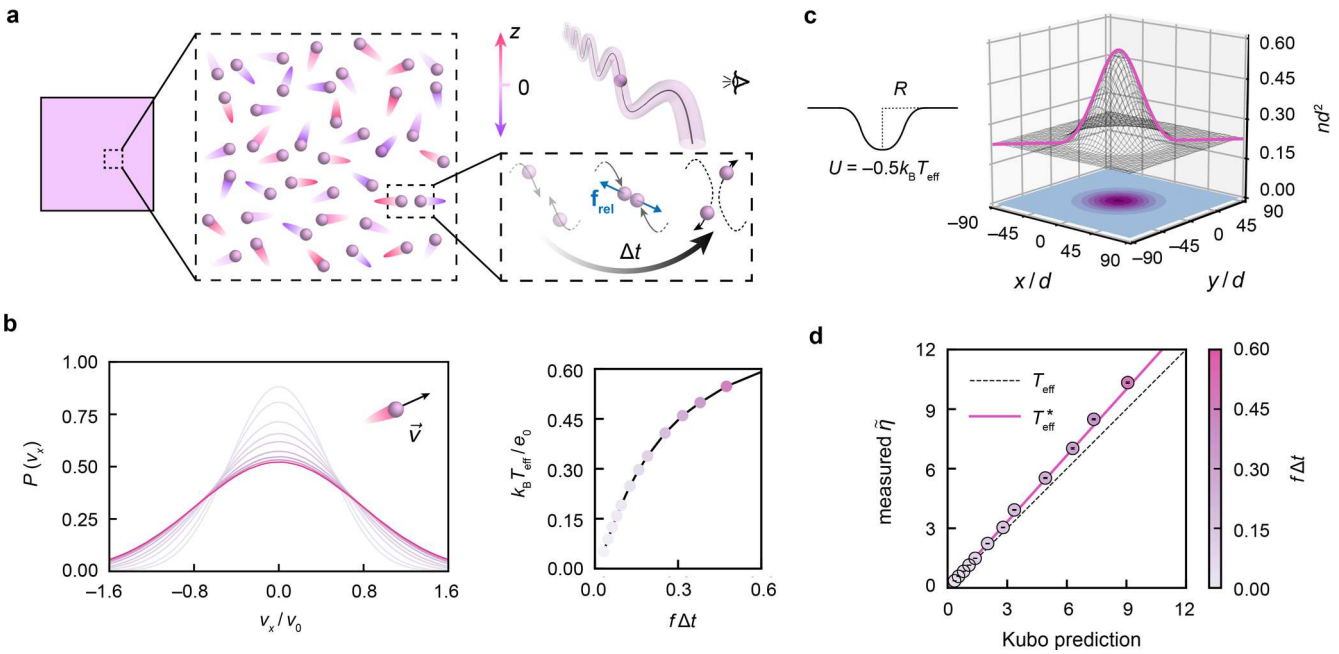

Extended Data Fig. 1 | Thermodynamics of an oscillating granular gas. a. Schematic of the system setup. We simulate a quasi-2D granular gas composed of frictional particles, which are forced to oscillate vertically at a constant frequency f but free to move horizontally. Interparticle collision between two oscillating particles could lead to their translational motions in the xy-plane. In the middle is a zoomed-in, top view of this many-body system. Horizontal translation of a particle is denoted by its tail, whereas its vertical oscillation is color-coded in the tail: gradient from a dark end to a bright front means the particle is moving towards the xy-plane, vice versa; purple denotes $z<0$ whereas red denotes $z>0$. Δt denotes the averaged collision duration. **b**. Maxwell distribution. The x-component of translational velocity displays a Gaussian distribution $P(v_x)$ at various oscillating frequency f. An effective temperature T_{eff} is defined using the halfwidth of $P(v_x)$. Dependence of T_{eff} on f is shown on the right. **c**. Boltzmann distribution. We put the system in a potential well $U(\mathbf{r}) = -0.5k_BT_{eff}\ [1+\cos(\pi r/R)]$ for $r<R$, where r denotes the distance from the center of the system. The resultant spatial distribution of the particles turns out to follow the Boltzmann statistics $n(-r) \propto \exp\ [-U(r)/k_BT_{eff}]$ (purple curve) as well. **d**. Green–Kubo relation. Shear viscosity of this many-body system can be either directly measured using linear response towards an applied shear or indirectly inferred from the Green–Kubo relation by calculating the integral of the stress–stress correlation function, known as the Green–Kubo relation. The predicted and measured shear viscosity η is compared at a wide range of frequencies f. The Kubo predictions with T_{eff} and renormalized T^*_{eff} are marked as the dashed and solid lines, respectively. We have defined $f_0 = 1/\Delta t$.

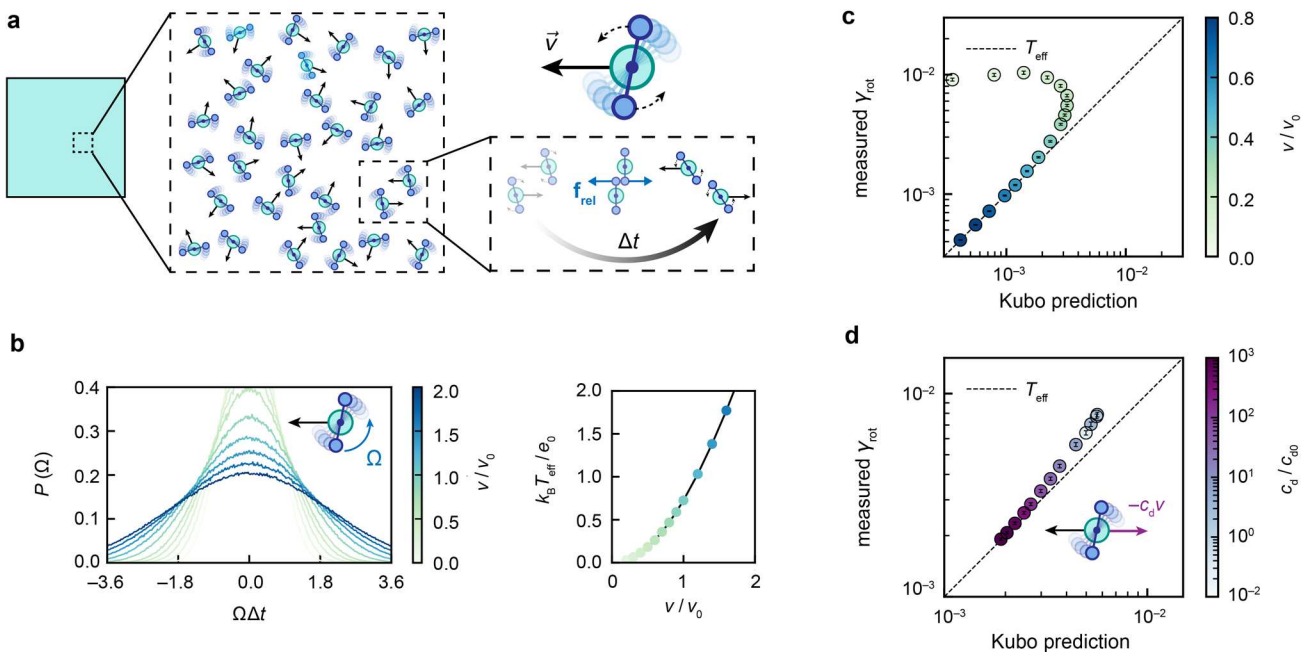

Extended Data Fig. 2 | Thermodynamics of an active Brownian system. a. Schematic of the system setup. We simulate a 2D system composed of active Brownian rollers. Each particle contains a core (in green) that self-propels nearly at a constant speed v meanwhile undergoes rotational diffusion as well as a dumbbell (in blue) that is hinged at the core center and free to rotate about it. In particular, the core of particle i is powered by an active force $\mathbf{F}_i^a = c_d v \hat{\mathbf{n}}_i$ ($\hat{\mathbf{n}}_i$ is the orientation of the core) meanwhile experiences a drag force by the substrate $\mathbf{F}_i^d = -c_d \mathbf{v}_i$, where ζ denotes the substrate friction coefficient. Note that the particle dumbbell is lifted away from the substrate thus does not experience any friction; moreover, the dumbbell rotation does not reorient the self-propulsion of the core. When two particles collide, the translational motion of the cores could result in the rotational motion of the dumbbells. Δt denotes the averaged collision duration. **b**. Maxwell distribution. The angular velocity of the dumbbells displays a Gaussian distribution $P(\Omega)$ at various self-propulsion speed v. An effective temperature T_{eff} is defined using the halfwidth of $P(\Omega)$. Dependence of T_{eff} on Ω is shown on the right. **c-d**. Green-Kubo relation. The rotational drag coefficient of the dumbbell can be either measured through linear response by measuring the terminal angular velocity under an applied torque, or predicted using the Green-Kubo relation by evaluating the integral of the torque–torque correlation function. The measured and predicted drag coefficient γ_{rot} is compared at a wide range of self-propulsion speed v (**c**) as well as substrate friction coefficient c_d (**d**). However, when either self-propulsion speed v or substrate friction coefficient c_d is increased, the relative significance of particle interaction compared to self-propulsion gets reduced. As a consequence, we see that the Green–Kubo relation is restored at either large v or c_d. We have defined $v_0 = d/\Delta t$ and $c_d = m/\Delta t$.

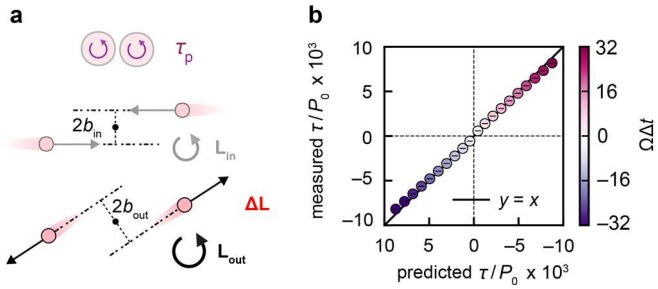

Extended Data Fig. 3 | Microscopic origin of anti-symmetric stress. a. Schematic of orbital angular momentum change during collision. When two frictional active spinners collide, the angular momentum of self-spinning can be interchanged with the angular momentum of orbital motion around their center-of-mass, $L = mv_{rel}b$, where v_{rel} is the relative moving speed of the particles and b is the impact parameter. The resultant change in the orbital angular momentum $\Delta L = L_{out} - L_{in}$ gives rise to effective anti-symmetric stress exerted onto the chiral active fluid at the macroscopic level. In the Supplementary Sec. III, we provide a simple kinetic theory to derive the linear relation between anti-symmetric stress τ and the average orbital angular momentum change $\overline{\Delta L}$ during collision, $\tau = \sqrt{\pi k_B T_{eff}/m} \cdot dn^2 \cdot \overline{\Delta L}$. **b**. Validation of our kinetic theory. We measure the average orbital angular momentum change $\overline{\Delta L}$ by performing scattering simulations and then use it to predict the anti-symmetric stress τ based upon the kinetic theory. The prediction on τ from $\overline{\Delta L}$ agrees well with the simulation measurement of a many-body system at the steady state.

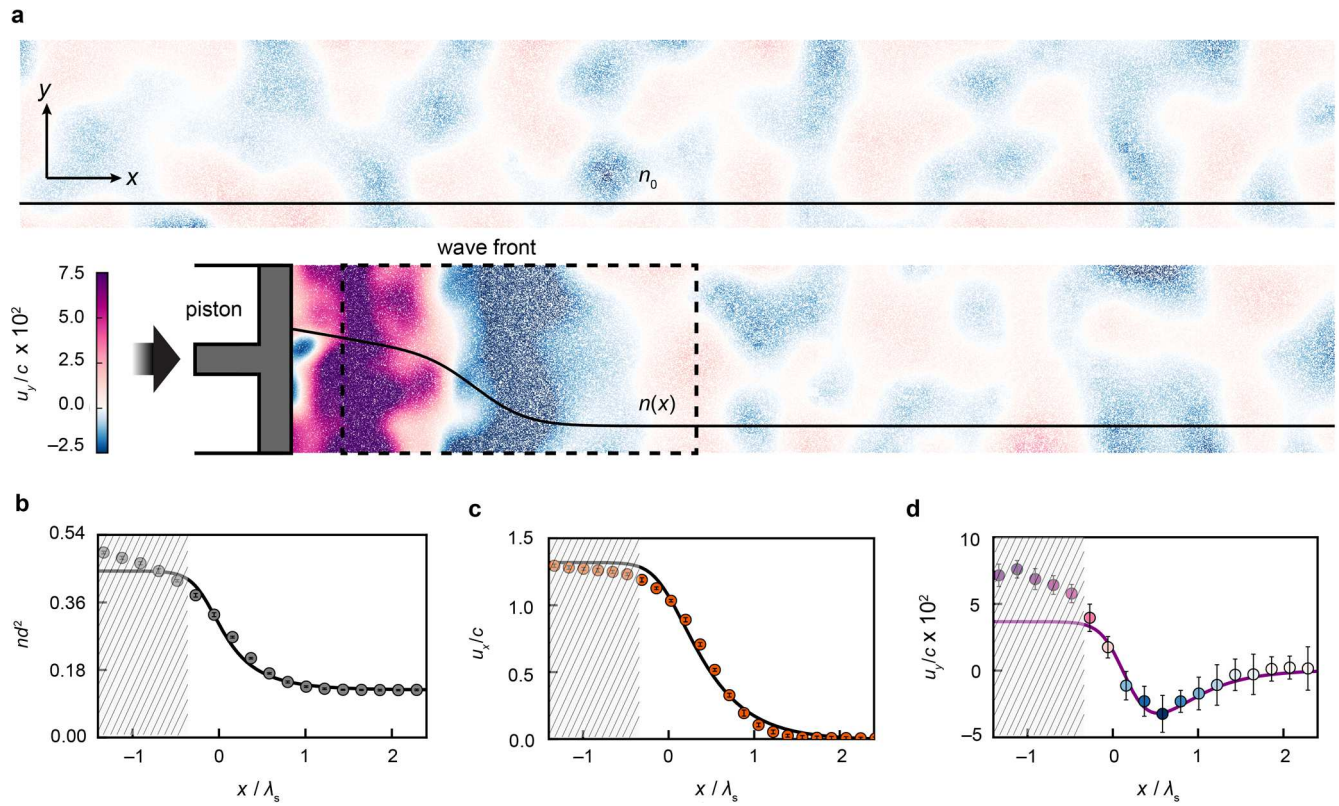

Extended Data Fig. 4 | Transverse mode in a shock wave. a. Shock wave. A piston moving at speed $U=1.9d/\Delta t$ (faster than the speed of sound $c=1.4d/\Delta t$) generates a shock wave accompanied with transverse flows, which is characterized by the vertical flow velocity u_y (gradient coloring). The particles self-spin counter-clockwise at speed $\Omega=25.3/\Delta t$ and have an initial global density $n_0=0.125d^{-2}$. According to the viscid Burgers' equation $\partial_t u + u\partial_x u = \nu\partial_x^2 u$, the width of this shock is approximately $\lambda_s=4\nu/U$, where $\nu=\eta/n_0 m$ is the kinematic viscosity. Hydrodynamic profiles are quantified near the wave front. Also see Supplementary Mov. S8. **b**. Density profile $n(x)$. The simulation results are compared with continuum hydrodynamic theory (solid line), which employs parameters measured in a separate homogeneous microscopic systems of number density n_0 (dashed line). Thus, theoretical predictions would break down at extreme densities (shaded region). **c**. Horizontal flow velocity $u_x(x)$. **d**. Vertical flow velocity $u_y(x)$. The same color coding as panel A is applied here. Predictions using continuum hydrodynamic theory are plotted as solid lines.

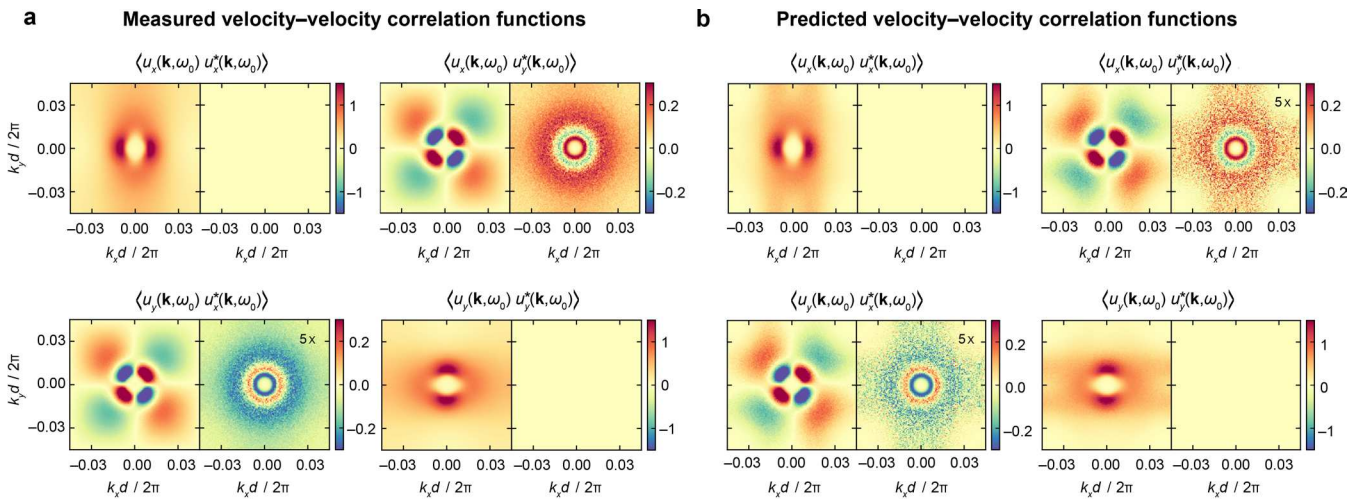

Extended Data Fig. 5 | Power spectra of the velocity–velocity correlation functions $\langle \boldsymbol{u}_a(\mathbf{k},\omega)\boldsymbol{u}_b^*(\mathbf{k},\omega)\rangle$**.** Here we compare the measured velocity–velocity correlation functions with the empirical prediction using fluctuating hydrodynamic theory. **a**. Correlation functions directly measured in the particle-based simulations of our chiral active fluid. **b**. Correlation functions predicted using the fluctuating hydrodynamic theory with the measured stress–stress correlation functions and viscosity tensor. The empirical prediction matches with the simulation results expect at very high k-modes, where the linear response approximation is no longer valid. Although the comparison is made at a given wave frequency $\omega_0 = 0.055\pi/\Delta t$, the consistency between direct measurements in simulations and predictions using fluctuating hydrodynamic theory generally holds at all wave frequencies.